



**1D AND 3D INVERSION AND MODELLING OF  
AIRBORNE TRANSIENT ELECTROMAGNETIC AND  
MAGNETIC DATA FROM OVER A POTENTIAL  
VOLCANOGENIC MASSIVE SULPHIDE DEPOSIT,  
CRIPPLE CREEK, NEWFOUNDLAND.**

by

Alican Demirbaş

A Thesis submitted to the School of Graduate Studies  
in partial fulfillment of the requirements for the degree of

Master of Science

Department of Earth Sciences  
Memorial University of Newfoundland

April, 2021

St. John's

Newfoundland and Labrador

## **ABSTRACT**

Electromagnetic (EM) methods, including Transient Electromagnetic (TEM), and magnetic methods, are commonly used in mineral exploration. In this study, EM and magnetic measurements are used to investigate possible mineralization zones in the Cripple Creek property in the Gander area, Newfoundland, Canada.

This study's main goal is to invert airborne TEM data for recovering the conductive structures of the mineralization zones in the area of interest. Airborne magnetic and ground-based frequency-domain EM data are also considered as supportive techniques, along with the TEM data-set. The magnetic results help define the regional geological structure of the area of interest. The ground-based frequency-domain EM, which exists over a limited area, and the TEM responses are compared and are shown to be mostly consistent. The geometry of a mineralized zone suggested by the TEM inversion is then refined by further computer modelling (using the software "Maxwell"). The resulting models are compared and discussed in terms of correctness of the inversion and the methods' effectiveness.

The results show that the 3D models of the conductivity interpolated from 1D inversion results of the TEM data recover the near-surface structures quite well but become inaccurate at depth. It is shown that the models resulting from the 3D magnetic inversion are partially consistent with the TEM results. This is possible

because of the physical property of the structure of interest, which means that the area of interest does not show the same magnetic properties everywhere. Both magnetic and TEM results are only overlapping on one of the flight lines, L2220. However, when the magnetic inversion is considered separately, it helps to reveal the magnetic properties reasonably well around the structure of interest.

## **GENERAL SUMMARY**

This study's main goal is to use the airborne electromagnetic (EM) data collected with a helicopter to reveal the mineralization zones that may include metal minerals such as copper, gold, and zinc in the area of interest called the core area in Cripple Creek Property. EM methods are commonly used in mineral exploration.

The EM data are processed to discover the structures, including minerals, under the Earth's surface, and the geology of the area is investigated for better understanding of the characteristic of the structure of interest.

Firstly, two different EM data-sets are compared with each other. Then EM data processing is carried out. After the TEM data's inversion, plate-like models are made and their responses computed approximately and all the work done is united and compared.

The EM data processing results show that the last Earth models of the area of interest generated through the modelling and processing recover the near-surface structures quite well but become inaccurate at depth. Magnetic data is also used in this study. It is shown that the Earth models resulting from the modelling of the magnetic data are partially consistent with the EM results. This is probably because of the physical properties of the structure of interest. The area does not show the same magnetic properties everywhere.



Both magnetic and TEM results are only overlapping on one of the flight lines, L2220. However, when the magnetic result is considered separately, it helps to reveal the magnetic properties fairly well surrounding the area of interest.

## **ACKNOWLEDGEMENTS**

Firstly, I would like to thank the Republic of Turkey Ministry of National Education for their sponsorship of me during this study. Thanks also to the Department of Natural Resources, Newfoundland and Labrador for providing me with the geophysical data used in this study.

Many thanks to my supervisor Prof. Colin G. Farquharson, for his guidance and support throughout these two years. Thanks to everyone under his supervision at the time but most importantly, Christopher George Galley for his help on the magnetic data modelling.

Finally, thank you so much to all the people at Memorial University for their academic and humanitarian support.

## TABLE OF CONTENTS

GENERAL SUMMARY .....	iv
ACKNOWLEDGEMENTS .....	vi
LIST OF FIGURES .....	ix
LIST OF TABLES .....	xiii
The Table of Abbreviations .....	xiv
1 Introduction .....	1
2 Theory of The Electromagnetic Method .....	6
2.1 EM Theory .....	6
2.1.1 Maxwell's Equations .....	6
2.1.2 The Behaviour of EM Fields in Conductors .....	9
2.1.3 Quasi-static Regime .....	18
2.1.4 Boundary and Interface Conditions .....	19
2.2 The Transient EM (TEM) Method .....	24
2.2.1 Overview .....	24
2.2.2 TEM Response over a layered Half-Space .....	27
2.2.3 Airborne TEM .....	29
2.3 Frequency-domain EM(FDEM) .....	32
2.4 The Magnetic Method .....	36
3 Modelling of Geophysical Data .....	40
3.1 Plate-modelling of EM Data .....	40
3.2 Inversion of Geophysical Data .....	44
3.3 1D TEM Inversion .....	48
3.4 Inversion codes used .....	52
3.4.1 1D TEM Inversion Code – EM1DTM .....	52
3.4.2 3D Magnetic Inversion code – VIDI .....	55
4 Survey Area .....	59
4.1 Geology .....	61
4.2 Mineralization .....	64
4.3 Previous Works .....	66
5 Prior to Inversion .....	70
6 Inversion and Modelling .....	80
6.1 1D Inversion of The Cripple Creek VTEM data .....	80
6.2 Maxwell Modelling .....	86
6.3 TEM 3D Modelling .....	92
6.4 3D Inversion of The Magnetic Data .....	96

7 Summary and Conclusion..... 102

REFERENCES ..... 105

Appendix A ..... 109

## LIST OF FIGURES

Figure 1.1 The location of the survey area (indicated by the red area) on the island of Newfoundland.....	2
Figure 2.1 (a) An EM wave in free space. (b) An EM “wave” in a conductor. The conductivity is $10 - 3 \text{ S/m}$ . Permeability, permittivity, and frequency values are $4\pi \times 10^{-7} \text{ H/m}$ , $8.85 \times 10^{-12} \text{ F/m}$ , and $105 \text{ Hz}$ respectively. The pictures are plotted using Eq. (2.10). The decaying of the EM wave in a conductor is seen in the picture (b). .....	14
Figure 2.2 The illustration of Eq. (2.25). The parameters of the waves are the same as in Figure 2.1b. It shows the phase difference between electric and magnetic fields, with the magnetic field lagging behind the electric field.....	17
Figure 2.3 3D illustration of exponential decaying of the electromagnetic waves in a conductive material and the lag between $E$ and $B$ field (Griffiths, 1999). .....	17
Figure 2.4 The measurement principles of the TEM method. (a) The current waveform in the transmitter loop. (b) The electromotive force in the subsurface. (c) The secondary magnetic field measured in the receiver and the time gates (Christiansen, 2006).....	25
Figure 2.5 An illustration of a TEM measurement. The blue dotted lines indicate the eddy currents generated by the transmitter loop. The solid blue loop on the surface is the transmitter, and the red one in the middle of the transmitter is the receiver coil. The green lines passing through the receiver coil represent the secondary magnetic fields generated by the eddy currents in the Earth (Africa, 2013).....	26
Figure 2.6 VTEM System Configuration. The receiver and the transmitter are at the bottom, and the GPS antenna and the magnetic sensor are at the top (Nahnybida and Willet, 2013). .....	30
Figure 2.7 A horizontal-loop frequency-domain system and its response over a conductive dike in a less conductive ground with a conductive overburden (McNeill, 1990).....	33
Figure 2.8 The in-phase and out-of-phase responses of a sphere to a frequency-domain system. Adapted from In-phase and out-of-phase response of a sphere, (n.d.).....	35
Figure 2.9 Magnetic susceptibilities for common mineral and rock types (adapted from Clark and Emerson 1991). .....	38

Figure 3.1 TEM responses over different plate-like conductors. The grey curves are the z-component of the response. The blue curves are the x-component of the response. (Adapted from Geotech Ltd. Report, 2012.) .....	42
Figure 3.2 TEM responses over different plate-like conductors. The grey curves are the z-component of the response. The blue curves are the x-component of the response. (Adapted from Geotech Ltd. Report, 2012.) .....	43
Figure 3.3 The horizontally layered conductivity model of the Earth. $z_j$ is the depth of the bottom of the $j$ th layer, $\sigma_j$ and $l_j$ are the conductivity and thickness of the layers, respectively. $S$ represents the source. (Modified from Farquharson and Oldenburg, 1993.).....	50
Figure 3.4 Two examples of inversion results of TEM soundings from the Cripple Creek data-set (Line 2290, 15 <sup>th</sup> and 60 <sup>th</sup> soundings).....	50
Figure 3.5 Rectilinear mesh example. The area of interest under the observation points is discretized using a rectilinear mesh. (Modified from Lelièvre, 2003). .....	55
Figure 4.1 The location of the Cripple Creek Property and Survey Lines. The black arrow shows the area of interest. (Retrieved from Google Earth.).....	60
Figure 4.2 Geology Map of Newfoundland and the location of the Cripple Creek Property shown by the red star ( <a href="https://www.gov.nl.ca/iet/files/mines-maps-nf.pdf">https://www.gov.nl.ca/iet/files/mines-maps-nf.pdf</a> ). .....	61
Figure 4.3 Regional geology of the Cripple Creek property. The red rectangle is the Core Area. (Adapted from Nahnybida and Willett, 2013.) .....	62
Figure 4.4 The geology and the rock chemistry map of the core area in the Cripple Creek Property. (Adapted from Nahnybida and Willett, 2013.) .....	63
Figure 4.5 Typical VMS occurrence at mid-ocean ridge (from Andrews, personal communication). .....	65
Figure 4.6 VMS deposit occurrence models in different structures (modified from Shanks and Thurston, 2010). .....	65
Figure 4.7 Geographical distribution of ancient VMS deposits (Galley et al., 2007).....	66
Figure 5.1 The Z component of the VTEM data for the whole of the Cripple Creek survey (Channel 40, see Table 4.1). Conductive trends, corresponding to the larger values on this map, are seen all over the Cripple Creek Property. The red rectangle shows the core area, and the black rectangle within the red one shows the area	

immediately surrounding the conductor of interest in this study. (Adapted from the Geotech Ltd. Report, 2012.) .....	73
Figure 5.2 The Total Magnetic Intensity (TMI) for whole Cripple Creek Property. The red rectangle shows the core area (and the magnetic data used), and the black rectangle in the red one shows the conductor of interest. The blue one shows the area for the inversion (Adapted from the Geotech Ltd. Report, 2012.) .....	75
Figure 5.3 Comparison of the TEM and HLEM responses along one pair of co-incident lines. The z-component of the TEM response for line L2290 is shown at the top. The HLEM response for line 11700 is shown at the bottom. See Figure A-1 for the locations of these two survey lines. The coloured lines on the top plot are the time gates in Table 5.1. The red and green lines on the lower plot represent the out-of-phase and in-phase components at 1760 Hz. ....	76
Figure 5.4 Comparison of the TEM and HLEM responses along one pair of co-incident lines. The z-component of the TEM response for line L2310 is shown at the top. The HLEM response for line 11500 is shown at the bottom. See Figure A-1 for the locations of these two survey lines. The coloured lines on the top plot are the time gates in the Table 5.1. The red and green lines on the lower plot represent the out-of-phase and in-phase components at 1760 Hz.....	77
Figure 6.1 2D cross-sections made from the TEM 1D inversion results over the main area of interest (see Fig. 5.5 for the locations of the flight lines). The arrows show the location of the conductor. The colour bar shows the conductivity in log scale ( $S/m$ ). Larger values of these sections are given in Appendix A. ....	81
Figure 6.2 The fit between observed and predicted data. The green line and the blue line represent the predicted and the observed data, respectively. The red signs show the estimations of the error in the observations. The peaks and troughs on the observed data later than approximately 9ms result from the sign changes in the observations. The absolute values of the observations are plotted. ....	84
Figure 6.3 The observed and predicted data of the L2290 and the L2310 survey lines. Ten soundings over the location of the conductor are used. The blue points and the red circles represent the predicted and the observed data, respectively. ....	85
Figure 6.4 The airborne TEM synthetic response over a Maxwell model and the airborne TEM observed response for line L2290 (top). The ground HLEM synthetic response over another Maxwell model and the ground HLEM observed response for survey line 11700 (bottom). The specifications of the models are given in Table 6.1. The red arrow shows the negative side-lobe values. ....	88

Figure 6.5 TEM (left; same as in Fig. 6.4) and HLEM responses (right) over the same model as for line L2290 (airborne TEM data).....	89
Figure 6.6 The airborne TEM synthetic response over a Maxwell model and the airborne TEM observed response for line L2310 (top). The ground HLEM synthetic response over another Maxwell model and the ground HLEM observed response for survey line 11500 (bottom). The specifications of the models are given in Table 6.2.....	91
Figure 6.7 3D images of the 1D TEM inversion result for survey lines L2310, L2290, and L2270. The red arrows show the conductor of interest.....	93
Figure 6.8 3D images of the 1D TEM inversion result for survey lines L2250, L2230, and L2210. The red arrows show the conductor of interest.....	94
Figure 6.9 3D images of the 1D TEM inversion result for survey lines L2190, L2170, and L2150. The red arrows shows the conductor of interest. ....	95
Figure 6.10 The mesh used for the 3D magnetic inversion. The top picture is the x-y section, along with the observation locations (red points). The coordinates of the corners of the top picture from top-two to bottom-two are 679900.6E - 5454749.5N, 686125.6E - 5454749.5N, and 679900.6E - 5448524.5N, 686775.6E - 5448524.5N. z-coordinates are 59.9 for all four points because the mesh has a flat surface. The bottom picture is the x-z cross-section view.....	98
Figure 6.11 a) The observed total-field magnetic anomaly. b) The normalized data misfit of the magnetic inversion under the observation points. ....	99
Figure 6.12 a) Plan view of the 3D magnetic inversion model. b) Geology map and the mineralization showing the core area. The red lines show the location of the conductor of interest that is dipping north-west.....	99
Figure 6.13 A slice through the 3D susceptibility model constructed by the magnetic inversion (at the top) and a slice through the 3D conductivity model from the 1D TEM inversion results (at the bottom). The slices are along survey line L2220. The black arrows show the conductor of interest. The units of the easting, northing, and depth are metres. The unit of the conductivity is $S/m$ . ....	101



## LIST OF TABLES

Table 5-1 TEM data decay sampling scheme.....	72
Table 6.1 The specifications of the Maxwell models for the TEM survey line L2290 and the HLEM survey line 11500.....	87
Table 6.2 The specifications of the Maxwell models for the TEM survey line L2310 and the HLEM survey line 11700.....	90

## The Table of Abbreviations

1D	1 Dimensional
2D	2 Dimensional
3D	3 Dimensional
Ag	Silver
As	Arsenic
Au	Gold
Bi	Bismuth
Cd	Cadmium
Co	Cobalt
Cu	Copper
EM	Electromagnetic
Ga	Gallium
Ge	Germanium
Hg	Mercury
In	Indium
Mn	Manganese
MT	Magnetotelluric
Pb	Lead
Sb	Antimony

Se	Selenium
Sn	Tin
Te	Tellerium
TEM	Transient Electromagnetic
VMS	Volcanogenic Massive Sulphide
VTEM	Versatile Transient Electromagnetic
Zn	Zinc

# 1 Introduction

Electromagnetic methods, including time-domain (TEM) and frequency-domain, and magnetic methods are commonly used in mineral exploration. In this study, airborne TEM, ground-based frequency-domain, and magnetic measurements are used to detect mineralization zones on the Cripple Creek property, near Gander in Newfoundland, Canada.

Data collected using Geotech's Versatile Transient Electromagnetic (VTEM) system over the Cripple Creek property is used. The VTEM system is an airborne measurement system including the separate TEM transmitter and receiver along with a magnetic sensor. The airborne TEM data-set is used as the main geophysical method in this research, and the magnetic and ground-based frequency-domain EM data-sets are used as supportive methods.

The Cripple Creek property is located in the east of Newfoundland, Canada, 20 km north of the town of Gander (see Figure 1.1). The property covers two tectonostratigraphic zones, the Dunnage Zone and the Gander Zone. The Gander River Complex is the formation between these two zones, an ophiolite comprising ultramafic to felsic plutonic rocks and mafic volcanic rocks. The Davidsville Group includes a basal conglomerate overlying the Gander River Complex. An upper unit comprises turbiditic greywacke and slate with minor limestone and sandstone. Upper Llanviran and Lower Llandeilo fossils found in

the limestone show a middle Ordovician age of deposition (O'Neill, 1991, as cited in Nahnybida and Willett, 2013).



Figure 1.1 The location of the survey area (indicated by the red area) on the island of Newfoundland.

The main possible mineralization in the Cripple Creek area is volcanogenic massive sulphide (VMS). The VMS mineralization occurs as lenses of massive polymetallic sulphide that form at or near the seafloor in submarine volcanic environments (Galley et al., 2007). VMS deposits actively form in the seafloor environment all over the world, known as modern VMS deposits, or have formed

throughout the years known as ancient VMS deposits. Newfoundland is a place that includes ancient VMS deposits.

VMS deposits are major sources of Zn, Cu, Pb, Ag, and Au, and significant resources for Co, Sn, Se, Mn, Cd, In, Bi, Te, Ga, and Ge. Some also include As, Sb, and Hg. VMS deposits make up 27% of Canada's Cu production, 49% of its Zn, 20% of its Pb, 40% of its Ag, and 3% of its Au (Galley et al., 2007).

Exploration in the Cripple Creek area dates back to the 1930s when interest was in finding a chromite deposit. Since then, a couple of drilling programs have been conducted, and many grab samples have been collected. In light of the previous work, a comprehensive geophysical study was carried out in 2012. An airborne time-domain EM survey, which included magnetic measurements, along with a ground-based horizontal loop frequency-domain EM survey, was conducted.

TEM systems have been used in mineral exploration since the 1950s. However, these systems did not become truly popular until the development of commercial systems in the 1970s. TEM methods are used directly as a main geophysical method in mineral exploration as well as for the support of other methods such as MT for static shift correction.

The TEM method is a controlled-source EM method that measures the magnetic response of induced eddy currents within the Earth. The TEM technique induces these electrical currents in the Earth using electromagnetic induction. An abrupt

shut-off of a current in a transmitter loop, in the air or on the ground, causes a time-varying magnetic field that induces the currents in the ground.

For the airborne TEM method, 1D inversion is often implemented due to the computational complexity of EM methods and the time-consuming nature of 2D and 3D modelling and inversion. One reason to use 1D inversion for airborne TEM data-sets is that it is computationally feasible for giant data-sets like the one considered in this study. 1D inversion recovers conductivity models only changing with depth beneath an observation location. 1D inversions have been found to still give useful results when the geology is not 1D. However, for complex geological structures, further investigations might be required.

The magnetic data are inverted in 3D for the whole “core area” not just over the immediate area of interest aiming to get valuable information about geological formations surrounding the mineralized zone. 3D inversion of magnetic data is not as computationally expensive as 2D or 3D modelling and inversion of EM data. Also, magnetic data and their inversion gives more of a regional picture of the geology rather than of the mineralized zone.

In Chapter 2, the theory of EM methods and the magnetic method is discussed. TEM responses over a layered half-space model and an overview of airborne TEM methods are addressed. A summary of the frequency-domain EM method is also given.

In Chapter 3, modelling and inversion of geophysical data are presented. The plate modelling, which provides a fast interpretation without inversion, is given. Inversion is presented at first in general, followed by 1D inversion of TEM data in particular. Lastly, in this chapter, the inversion codes used in this research are described in detail.

In Chapter 4, after giving the geological background of the survey area, the main mineralization type, which is volcanogenic massive sulphide (VMS), is described along with examples from Canada. As well, in the latter part of this chapter, the processes that are required prior to inversion are presented. The TEM responses over the mineralized zones are compared with the frequency-domain EM responses. Plate-based EM modelling is done using the program Maxwell, and the consistency between the results of the various interpretation methods discussed.

In Chapter 5, 1D TEM and 3D magnetic inversion results are both presented. In Chapter 6, the constructed inversion models are given along with the data residuals to show how the inversion is reliable. And, Chapter 7 presents the conclusions resulting from the work done for this thesis.



## 2 Theory of The Electromagnetic Method

### 2.1 EM Theory

#### 2.1.1 Maxwell's Equations

Electromagnetic geophysical methods are all based upon the fact that a magnetic field varying in time, according to Maxwell's equations, induces an electrical current in any nearby conductors. The differential forms of Maxwell's equations for a source-free region are (Griffiths, 1999):

$$\nabla \times \mathbf{e} + \frac{\partial \mathbf{b}}{\partial t} = 0 \quad (2.1a)$$

$$\nabla \times \mathbf{h} - \frac{\partial \mathbf{d}}{\partial t} = \mathbf{j}, \quad (2.1b)$$

$$\nabla \cdot \mathbf{b} = 0, \quad (2.1c)$$

$$\nabla \cdot \mathbf{d} = \rho \quad (2.1d)$$

in which

$\mathbf{j}$  is the electric current density in  $A/m^2$ ,

$\rho$  is electric charge density in  $C/m^3$ ,

$\mathbf{e}$  is the electric field intensity in  $V/m$ ,

$\mathbf{b}$  is the magnetic induction in  $(Wb/m^2 \text{ or Tesla})$ ,

**d** is the dielectric displacement in  $C/m^2$ , and

**h** is the magnetic field intensity in  $(A/m)$ .

According to Eq. (2.1a), i.e., Faraday's Law, a time-varying magnetic field induces an electric field that is perpendicular to the magnetic field. Ampere's Law, Eq. (2.1b) expresses that magnetic fields are the results of the sum of conduction currents and displacement currents and occur perpendicular to the currents. Eq. (2.1c), i.e., Gauss's Law, specifies that the magnetic fields are bipolar, and the last equation, Gauss Law for electric fields, tells us that electric fields are monopolar.

Maxwell's equations are not entirely sufficient to explain the electromagnetic phenomena in materials. (For conductivities of different materials, see Table 2.1). Constitutive relations are required to define electromagnetic phenomena more clearly that determine the physical properties of the materials. Maxwell's equations can be associated using constitutive relations in the frequency-domain (Ward and Hohmann, 1988):

$$\mathbf{D} = \varepsilon(\omega, \mathbf{E}, r, t, T, P, \dots) \mathbf{E}, \quad (2.2a)$$

$$\mathbf{B} = \mu(\omega, \mathbf{H}, r, t, T, P, \dots) \mathbf{H}, \quad (2.2b)$$

$$\mathbf{J} = \sigma(\omega, \mathbf{E}, r, t, T, P, \dots) \mathbf{E}, \quad (2.2c)$$

where  $\varepsilon$ ,  $\mu$  and  $\sigma$  are the electric permittivity, the magnetic permeability, and the electrical conductivity respectively as functions of angular frequency  $\omega$ , electric field strength  $\mathbf{E}$  or magnetic induction  $\mathbf{B}$ , position  $r$ , time  $t$ , temperature  $T$ , and pressure  $P$ . The reason that upper-case letters are used in Eq. (2.2) is that they were used to represent frequency-domain here, in contrast to the time-domain version of the equations given in Eq. (2.1).

In most elementary electromagnetic Earth problems, the following assumptions are made to simplify analysis (Ward and Hohmann, 1988):

- All media are linear, which means that the properties do not depend on the strength of the electric and magnetic fields. These fields are isotropic, homogeneous, and possess electric properties that are independent of frequency, time, temperature, or pressure.
- The magnetic permeability  $\mu$  is assumed to be that of free space.

After these assumptions, we can define three constitutive relations more simply:

$$\mathbf{D} = \varepsilon \mathbf{E} \quad (2.3a)$$

$$\mathbf{B} = \mu \mathbf{H}, \quad (2.3b)$$

$$\mathbf{J} = \sigma \mathbf{E} \quad (2.3c)$$

### 2.1.2 The Behaviour of EM Fields in Conductors

In free space, free charge density  $\rho_f$ , which means the charges that are more likely to generate a current than bound charges, and the free current density  $J_f$  are zero. This restriction is reasonable for electromagnetic waves propagating through a vacuum or through insulating materials in which there is no free charge. However, in conductors, the flow of charge is not prevented, and  $J$  is certainly not zero. In fact, according to Ohm's Law, Eq. 2.3c, the free current density in a conductor is proportional to the electric field:

$$\mathbf{j}_f = \sigma \mathbf{e}. \quad (2.4)$$

Hence, Maxwell's equations for linear conductive media can be written as

$$\nabla \times \mathbf{e} = -\frac{\partial \mathbf{b}}{\partial t}, \quad (2.5a)$$

$$\nabla \times \mathbf{b} = \mu \sigma \mathbf{e} + \mu \epsilon \frac{\partial \mathbf{e}}{\partial t}, \quad (2.5b)$$

$$\nabla \cdot \mathbf{e} = \frac{\rho_f}{\epsilon}, \quad (2.5c)$$

$$\nabla \cdot \mathbf{b} = 0. \quad (2.5d)$$

There is also the continuity equation for free charge,

$$\nabla \cdot \mathbf{j}_f = -\frac{\partial \rho_f}{\partial t}. \quad (2.6)$$

Together with Ohm's Law (Eq. 2.3c) and Gauss's Law (Eq. 2.5c), gives

$$\frac{\partial \rho_f}{\partial t} = -\sigma(\nabla \cdot \mathbf{e}) = -\frac{\sigma}{\epsilon} \rho_f.$$

for a homogeneous linear medium. It follows from the above equation that

$$\rho_f(t) = e^{-(\sigma/\epsilon)t} \rho_f(0). \quad (2.7)$$

Therefore, any initial free charge density  $\rho_f(0)$  dissipates in a characteristic time  $\tau \equiv \epsilon/\sigma$ . This means that if we put some free charge on a conductor, it will flow out to the edges (Griffiths, 1999). The time constant  $\tau$  refers to a measure of how good a conductor is. It is clear that the free charge density decreases at a rate based on the exponential in Eq. 2.7. Since this time is not important to express the behavior of the EM field, it can be assumed that free charge density is zero.

When  $\rho_f = 0$ , Maxwell's equations can be written as

$$\nabla \times \mathbf{e} = -\frac{\partial \mathbf{b}}{\partial t}, \quad (2.8a)$$

$$\nabla \times \mathbf{b} = \mu\sigma\mathbf{e} + \mu\epsilon\frac{\partial \mathbf{e}}{\partial t}, \quad (2.8b)$$

$$\nabla \cdot \mathbf{e} = 0, \quad (2.8c)$$

$$\nabla \cdot \mathbf{b} = 0. \quad (2.8d)$$

Applying the curl to (2.8a) and (2.8b) gives the wave equations for  $E$  and  $B$ :

$$\nabla^2 \mathbf{e} = \mu\epsilon \frac{\partial^2 \mathbf{e}}{\partial t^2} + \mu\sigma \frac{\partial \mathbf{e}}{\partial t} \quad \nabla^2 \mathbf{b} = \mu\epsilon \frac{\partial^2 \mathbf{b}}{\partial t^2} + \mu\sigma \frac{\partial \mathbf{b}}{\partial t}. \quad (2.9)$$

These equations have plane-wave solutions:

$$\mathbf{e}(z, t) = \mathbf{E}_0 e^{i(kz - \omega t)}, \quad \mathbf{b}(z, t) = \mathbf{B}_0 e^{i(kz - \omega t)}. \quad (2.10)$$

Because the “wave number”  $k$  is complex:

$$k^2 = \mu\epsilon\omega^2 + i\mu\sigma\omega, \quad (2.11)$$

by substituting Eq. (2.10) into the Eq. (2.9) and taking the square root,

$$k = k_1 + ik_2, \quad (2.12)$$

where

$$k_1 \equiv \omega \sqrt{\frac{\mu\epsilon}{2}} \left[ \sqrt{1 + \left(\frac{\sigma}{\epsilon\omega}\right)^2} + 1 \right]^{1/2}, \quad k_2 \equiv \omega \sqrt{\frac{\mu\epsilon}{2}} \left[ \sqrt{1 + \left(\frac{\sigma}{\epsilon\omega}\right)^2} - 1 \right]^{1/2}. \quad (2.13)$$

The imaginary part of  $k$  results in an attenuation of the wave (decreasing amplitude with increasing distance):

$$\mathbf{e}(z, t) = \mathbf{E}_0 e^{-k_2 z} e^{i(k_1 z - \omega t)}, \quad \mathbf{b}(z, t) = \mathbf{B}_0 e^{-k_2 z} e^{i(k_1 z - \omega t)}. \quad (2.14)$$

The distance over which the amplitude decreases by a factor of  $1/e$  is called the skin depth:

$$\delta \equiv \frac{1}{k_2}. \quad (2.15a)$$

It is a measure of how far the wave penetrates into the conductor. As can be seen from Eq. (2.13), the skin depth is a fairly complicated function depending on the frequency and the physical properties of the media. Table (2.1) shows skin depths for certain rocks at various frequencies. It should not be forgotten that this Table is a general guide since the rocks can be classified by many different physical properties.

Table 2.1 Conductivities and skin depths of various materials. Adapted from Attenuation and Skin Depth (n.d.).

Type	$\sigma \left( \frac{S}{m} \right)$	$\mu_r$	$\epsilon_r$	$\delta(1\text{Hz})$	$\delta(1\text{kHz})$	$\delta(1\text{MHz})$
Air	0	1	1	$\infty$	$\infty$	$\infty$
Sea water	3.3	1	80	277 m	8.76 m	0.277 m
Igneous	$10^{-4}$	1	5	50,300 m	1,590 m	121 m
Sedimentary(dry)	$10^{-3}$	1	4	15,900 m	500 m	18 m
Sedimentary(wet)	$10^{-2}$	1	25	5,000 m	160 m	5.4 m

Sulphide Skarn	$10^2$	1	5	50 m	1.6 m	0.05 m
Magnetite Skarn	$10^2$	2	5	36 m	1.1 m	0.04 m

In the quasi-static approximation, for which  $\varepsilon\omega \ll \sigma$ , the skin depth is equal to

$$\delta = \sqrt{\frac{2}{\omega\mu\sigma}}. \quad (2.15b)$$

Assuming the Earth is non-magnetic and replacing  $\omega = 2\pi f$ , a more straightforward form of the skin depth formula is given by:

$$\delta \approx 503 \sqrt{\frac{1}{f\sigma}} = 503 \sqrt{\frac{\rho}{f}}. \quad (2.15c)$$

Ward and Hohmann (1988) give a time-domain skin depth

$$\delta \approx \sqrt{\frac{2t}{\mu\sigma}} \quad (2.15d)$$

where  $t$  is the time after decay has started.

Eq. (2.10) and Eq. (2.14) show that electric and magnetic fields behave like a sine or cosine function in free space, but in a conductor, they decay exponentially. In Eq. (2.10), electric and magnetic fields are represented with complex values. In Eq. (2.14)  $k_1$  and  $k_2$  are real numbers. Eq. 2.10 and 2.14 are



the same, and they are illustrated in Fig. 2.1 for free space and a conductor, respectively.

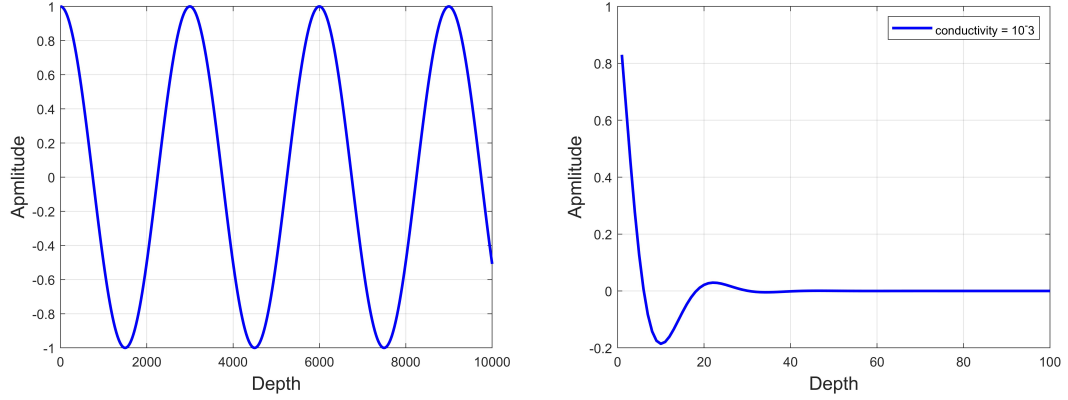


Figure 2.1 (a) An EM wave in free space. (b) An EM “wave” in a conductor. The conductivity is  $10^{-3} \text{ S/m}$ . Permeability, permittivity, and frequency values are  $4\pi \times 10^{-7} \text{ H/m}$ ,  $8.85 \times 10^{-12} \text{ F/m}$ , and  $10^5 \text{ Hz}$  respectively. The pictures are plotted using Eq. (2.10). The decaying of the EM wave in a conductor is seen in the picture (b).

Meanwhile, the real part of  $k$  determines the wavelength, the propagation speed, and the index of refraction in the usual way:

$$\lambda = \frac{2\pi}{k_1}, v = \frac{\omega}{k_1}, n = \frac{ck_1}{\omega}. \quad (2.16)$$

The attenuated plane waves (Eq. 2.14) satisfy the modified wave equations (Eq. 2.9) for any  $E_0$  and  $B_0$ . However, Maxwell’s equations (Eq. 2.8) bring further limitations, which are the determinations of the relative amplitudes, phases, and polarizations of  $\mathbf{e}$  and  $\mathbf{b}$ . We may orient the axes so that  $\mathbf{e}$  is polarized along the x-direction and  $\mathbf{b}$  is polarized along the y-direction:

$$\mathbf{e}(z, t) = E_0 e^{-k_2 z} e^{i(k_1 z - \omega t)} \hat{\mathbf{x}}, \quad (2.17)$$

$$\mathbf{b}(z, t) = \frac{k}{\omega} E_0 e^{-k_2 z} e^{i(k_1 z - \omega t)} \hat{\mathbf{y}}. \quad (2.18)$$

The electric and magnetic fields are mutually perpendicular.

Like any complex number,  $k$  can be expressed in terms of its modulus and phase:

$$k = K e^{i\Phi}, \quad (2.19)$$

where

$$K \equiv |k| = \sqrt{k_1^2 + k_2^2} = \omega \sqrt{\mu\epsilon} \sqrt{1 + \left(\frac{\sigma}{\epsilon\omega}\right)^2}, \quad (2.20)$$

and

$$\Phi \equiv \tan^{-1}(k_2/k_1). \quad (2.21)$$

According to Equations (2.17) and (2.18), the complex amplitudes  $E_0 = E_0 e^{i\delta_E}$  and  $B_0 = B_0 e^{i\delta_B}$  are related by

$$B_0 e^{i\delta_B} = \frac{K e^{i\Phi}}{\omega} E_0 e^{i\delta_E}. \quad (2.22)$$

Obviously, the electric and magnetic fields are no longer in phase; in fact,

$$\delta_B - \delta_E = \Phi, \quad (2.23)$$

which means that the magnetic field lags behind the electric field. Meanwhile, the real amplitudes of  $\mathbf{e}$  and  $\mathbf{b}$  are related by

$$\frac{b_0}{e_0} = \frac{K}{\omega} = \sqrt{\mu\epsilon} \sqrt{1 + \left(\frac{\sigma}{\epsilon\omega}\right)^2}. \quad (2.24)$$

The real electric and magnetic fields are,

$$\mathbf{e}(z, t) = E_0 e^{-k_2 z} \cos(k_1 z - \omega t + \delta_E) \hat{\mathbf{x}}, \quad (2.25a)$$

$$\mathbf{b}(z, t) = B_0 e^{-k_2 z} \cos(k_1 z - \omega t + \delta_E + \Phi) \hat{\mathbf{y}}. \quad (2.25b)$$

These fields are shown in Fig. 2.2 and 2.3.

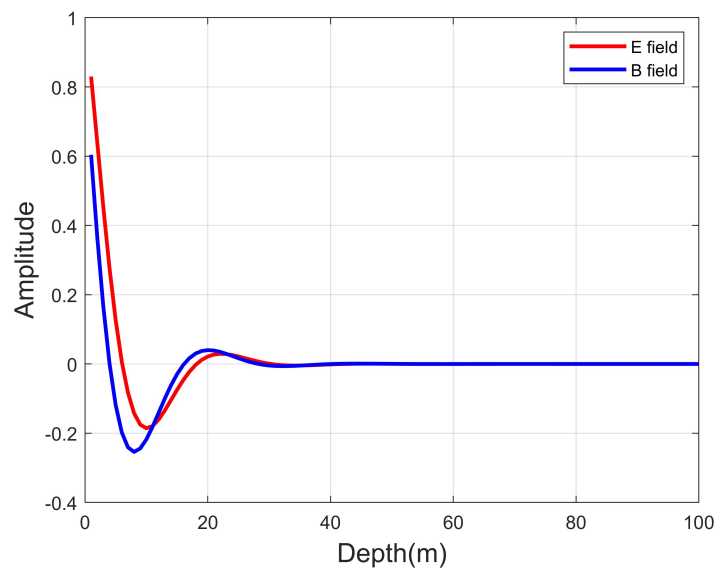


Figure 2.2 The illustration of Eq. (2.25). The parameters of the waves are the same as in Figure 2.1b. It shows the phase difference between electric and magnetic fields, with the magnetic field lagging behind the electric field.

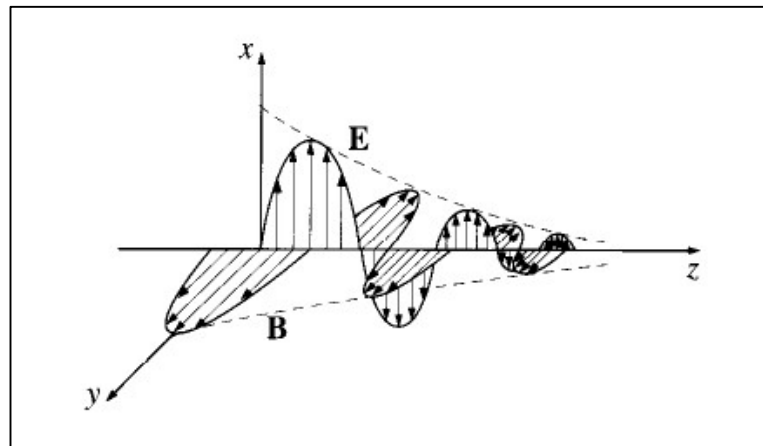


Figure 2.3 3D illustration of exponential decaying of the electromagnetic waves in a conductive material and the lag between  $E$  and  $B$  field (Griffiths, 1999).

### 2.1.3 Quasi-static Regime

Geophysical EM induction methods, TEM or FDEM, work in a quasi-static environment. This means that for low frequencies, less than 1MHz, according to Nabighian and Macnae (1991), any magnetic field generated by displacement current is negligible, and the magnetic field measured at the receiver is due only to conduction currents.

Considering again Eq. (2.9):

$$\nabla^2 \mathbf{b} - \mu\sigma \frac{\partial \mathbf{b}}{\partial t} - \mu\epsilon \frac{\partial^2 \mathbf{b}}{\partial t^2} = 0.$$

In this equation, the first term is called the Laplacian ( $\nabla^2$ ) and involves the spatial derivatives of the magnetic field. The second term describes the diffusive nature of the EM signal. For most materials in the ground  $\mu \approx \mu_0$ . Hence, in the quasi-static regime, the diffusive term is much larger than the conservation term, i.e.:

$$\sigma \frac{\partial \mathbf{b}}{\partial t} \gg \epsilon \frac{\partial^2 \mathbf{b}}{\partial t^2}.$$

And thus, the equation for the magnetic field can be written as

$$\nabla^2 \mathbf{b} - \mu\sigma \frac{\partial \mathbf{b}}{\partial t} = 0.$$

We can conclude from the last equation here that the diffusive properties of EM signals dominate, and depend on the conductivity.

### 2.1.4 Boundary and Interface Conditions

The equations in the previous section govern how EM fields behave in a uniform medium. However, to solve geophysical problems, it is essential to know how EM fields behave at the boundaries between media with different electrical properties. To achieve that, the integral form of Maxwell's equations in the time domain can be written as:

$$\oint_C \mathbf{e} \cdot d\mathbf{l} = - \int_S \frac{\partial \mathbf{b}}{\partial t} \cdot d\mathbf{s} \quad (2.26a)$$

$$\oint_C \mathbf{h} \cdot d\mathbf{l} = \int_S \left( j + \frac{\partial \mathbf{d}}{\partial t} \right) \cdot d\mathbf{s} \quad (2.26b)$$

$$\int_S \mathbf{d} \cdot d\mathbf{s} = \int_V \mathbf{\rho} \cdot d\mathbf{v} \quad (2.26c)$$

$$\oint_S \mathbf{b} \cdot d\mathbf{s} = 0 \quad (2.26d)$$

#### 2.1.4.1 Normal Components at the Interface

Consider a boundary between two media with different electrical properties:  $\varepsilon_1\mu_1\sigma_1$  and  $\varepsilon_2\mu_2\sigma_2$  for media 1 and media 2, respectively. To determine the behavior of the fields at the boundary  $S$  between the media, an extremely small Gaussian pillbox of height  $h$  and area  $S$  that crosses the interface is constructed. Eq. (2.26d) is evaluated here over the top and the bottom of the pillbox giving (for detailed information, see Interface Conditions in the references):

$$n \cdot (b_2 - b_1) = 0. \quad (2.27)$$

This means that the normal component of the magnetic intensity will be continuous across the interface.

Electric displacement with Eq. (2.26c) may be considered similarly as magnetic intensity:

$$n \cdot (d_2 - d_1) = \rho_s, \quad (2.28)$$

in which  $\rho_s$  is the surface charge density. This states that the normal component of the electric displacement is discontinuous at an interface.

To obtain the interface condition of the normal components for the electric field density, Eq. (2.3a) and (2.28) are combined:

$$\varepsilon_2 e_2 - \varepsilon_1 e_1 = \rho_s. \quad (2.29)$$

This equation means that the normal component of the electric field intensity is discontinuous at an interface.

To obtain the interface condition for normal components of the electric current density, Eq. (2.3c) and (2.29) are combined. Thus:

$$\frac{\varepsilon_1}{\sigma_1} j_1 - \frac{\varepsilon_2}{\sigma_2} j_2 = \rho_s. \quad (2.29)$$

This equation means that if the conductivities of the two materials is different, the normal component of the electric current density is discontinuous at an interface.

#### 2.1.4.2 Tangential Components at the Interface

Consider a Gaussian rectangle of height  $h$ , width  $l$ , and area  $A$  that straddles the interface. By applying Eq. (2.26a) to the rectangle, it is obtained the following:

$$-\int_S \frac{\partial \mathbf{b}}{\partial t} \cdot d\mathbf{s} = \oint_C \mathbf{e} \cdot d\mathbf{l} = e_1 \cdot (\Delta l) + e_2 \cdot (\Delta l).$$

This equation yields

$$\frac{\partial \mathbf{b}}{\partial t} hl = (e_1 - e_2) \cdot \Delta l.$$



By taking the limit  $h \rightarrow 0$  while the width  $l$  fixed, the left-hand side of the equation goes to zero. Thus, it can be written as

$$n \times (e_1 - e_2) = 0, \quad (2.30)$$

which means that the tangential component of the electric field is continuous across the interface.

The procedure to get the interface condition for the tangential component of the magnetic field is the same as that used to obtain the tangential component of the electric field. By considering a small rectangle, Eq. (2.26b), i.e., Ampere's law, is written as

$$n \times (h_1 - h_2) = \lim_{h \rightarrow 0} \left( j + \frac{\partial \mathbf{d}}{\partial t} \right) \Delta h.$$

The right-hand side of this equation goes to zero if there is only volumetric current. However, there is still the possibility that free current that flows along with the interface. Therefore, the equation turns into

$$n \times (h_1 - h_2) = j_s, \quad (2.31)$$

where  $j_s$  is the surface current. Therefore, the tangential component of the magnetic field can be discontinuous at an interface.

To obtain the interface condition for tangential components of the electric current density, Eq. (2.3a) and (2.30) are combined:

$$\frac{j_1}{\sigma_1} - \frac{j_2}{\sigma_2} = 0. \quad (2.32)$$

Hence, the tangential component of the current density is discontinuous at an interface.

However, for most materials in the ground, there is a volumetric current density and not a pure current surface density. Therefore, in practice, there is continuity of the tangential H-field. There is only a true surface current in a perfect conductor.

## **2.2 The Transient EM (TEM) Method**

### **2.2.1 Overview**

The Transient Electromagnetic Method (TEM), which is also known as time-domain EM (TDEM), is a controlled-source EM method that measures the evolution with time of the magnetic response of induced eddy currents within the Earth. The TEM technique induces electrical currents in the Earth using electromagnetic induction. A time-varying magnetic field is created by using a coil or loop of wire on the Earth's surface or in the air with a helicopter or fixed-wing aircraft. There are various loop configurations to implement this method. Yet, the in-loop system is emphasized in this work because of the fact that the real data considered in this study are obtained by using an in-loop system.

Faraday's law of induction tells us that a changing magnetic field produces an electric field and then an electric current in a conductive region. The current is turned on and then rapidly turned off in the transmitter so that the time-varying primary magnetic field is created around the transmitter and throughout the subsurface. The primary magnetic field induces a secondary electric current in the subsurface, which is called the eddy current. The eddy currents diffuse downward and outward, as can be seen in Fig. 2.4, while the amplitude of them decreases. Finally, the secondary magnetic field produced by those eddy

currents is measured by a magnetometer or as a voltage in an induction coil (see Fig. 2.4).

The data that is the secondary magnetic field is measured in time windows, which are often called time-gates (see Fig. 2.4). The length of the time-gates increases logarithmically with time to improve the signal-to-time ratio at late times. The measured signals at early times contain the conductivity information of the shallow layers, and the signals at late times contain the conductivity information of the deeper layers and/or more conductive features.

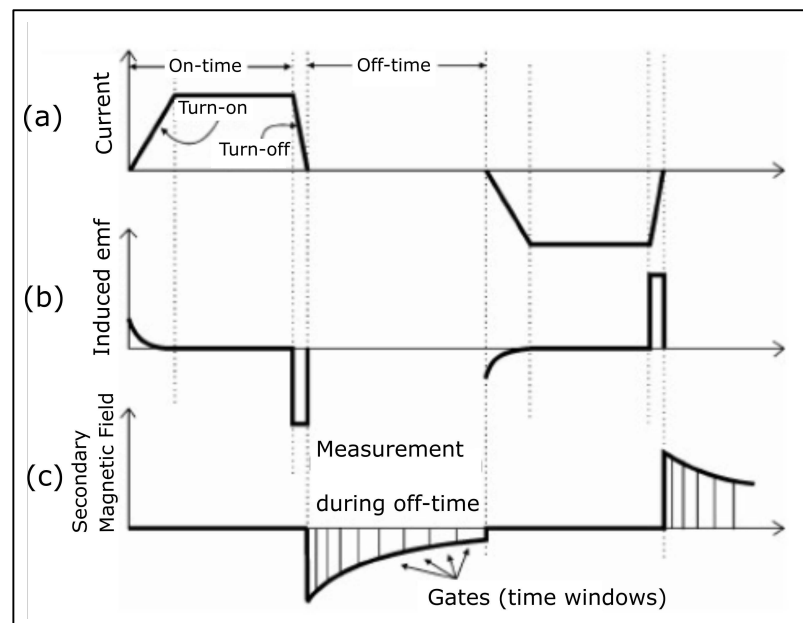


Figure 2.4 The measurement principles of the TEM method. (a) The current waveform in the transmitter loop. (b) The electromotive force in the subsurface. (c) The secondary magnetic field measured in the receiver and the time gates (Modified from Christiansen, 2006).

The measured secondary magnetic field generated by the eddy currents contains information about the conductive structures of the ground because the strength of the secondary current is based on the property of the Earth materials through which it goes.

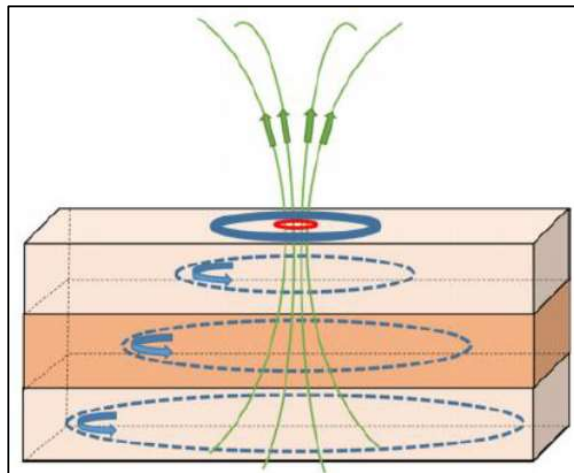


Figure 2.5 An illustration of a TEM measurement. The blue dotted lines indicate the eddy currents generated by the transmitter loop. The solid blue loop on the surface is the transmitter, and the red one in the middle of the transmitter is the receiver coil. The green lines passing through the receiver coil represent the secondary magnetic fields generated by the eddy currents in the Earth (Africa, 2013).

Time-domain techniques can be used for different aims. It is generally used to find out layered structures of geology, oil and groundwater exploration, high conductivity zones that might be associated with geothermal or massive sulphide targets, and for other mining exploration projects. The details about the usage of TEM are given in Nabighian and Macnae (1991).

### 2.2.2 TEM Response over a layered Half-Space

In the TEM technique, to express a derivation of the vertical magnetic field in the centre of a circular loop, the Schelkunoff Potential  $F$  can be used. The geometry of the situation gives fields in what is known as the transverse electric mode, for which the  $F$  potential is sufficient. Source-free regions on the surface or in the air and regions containing sources in the air or in the subsurface are present in geophysical problems. Hence, a derivation of the  $F$  potential requires the definition of source properties.

A transmitter loop can be represented as the integration of vertical magnetic dipoles over the area of the loop. The Schelkunoff potential for a vertical dipole is given by the Christiansen (2006):

$$F(\rho, z) = \frac{i\omega\mu_0 m}{4\pi} \int_0^\infty [e^{-u_0|z+h|} + r_{TE}e^{u_0(z-h)}] \frac{\lambda}{u_0} J_0(\lambda\rho) d\lambda \quad (2.33)$$

where

$m$  is the magnetic moment of the dipole,

$J_0$  is the Bessel function of order zero,

$\lambda = \sqrt{k_x^2 + k_y^2}$  where  $k_x$  and  $k_y$  are spatial frequencies or wavenumbers in the x- and y-directions,

$u_n = \sqrt{\lambda^2 - k_n^2}$  where  $k_n^2$  is the wavenumber in layer  $n$ ,

$\rho = \sqrt{x^2 + y^2}$  is the radial distance from the source to receiver, and

$r_{TE}$  is the complex reflection coefficient containing the material parameters of the subsurface.

Integrating Eq. (2.33) over a circular loop with radius  $a$  and current  $I$  yields

$$F(\rho, z) = \frac{i\omega\mu_0 Ia}{2} \int_0^\infty \frac{1}{u_0} [e^{-u_0|z+h|} + r_{TE}e^{u_0(z-h)}] J_1(\lambda a) J_0(\lambda \rho) d\lambda \quad (2.34)$$

where  $J_1$  is the first order Bessel Function.

Eq. (2.34) is applied for a circular transmitter loop with the dipole receiver at the distance  $\rho$  from the centre of the loop. In the central loop system used in this research,  $\rho$  is considered to be zero.

After some adjustments, according to Christiansen (2006), the vertical magnetic field at the receiver in a central loop configuration can be expressed as

$$F(\rho, z) = \frac{Ia}{2} \int_0^\infty [e^{-u_0|z+h|} + r_{TE}e^{u_0(z-h)}] \frac{\lambda^2}{u_0} J_1(\lambda a) d\lambda. \quad (2.35)$$

Eq. (2.35) is expressed in the frequency domain. To obtain the time-domain response, a Fourier transform or Laplace transform is used.

### **2.2.3 Airborne TEM**

The first airborne TEM systems were used in the 1950s in Canada to explore for minerals in fairly large areas. In the subsequent years, different TEM systems have been developed for mineral exploration to detect deep conducting targets, and airborne frequency-domain systems have been developed for near-surface exploration with high resolution (Christiansen, 2006).

Even though there are a lot of transmitter-receiver loop system configurations in TEM techniques, the central loop system, or in-loop, is extensively used. The advantages of central loop systems, particularly in the airborne systems, are simplified navigation and operation because the transmitter and receiver are in one compact unit that is more easily applied. Also, a GPS sensor and a magnetometer can be added to this compact unit to give accurate positioning of the transmitter and receiver and to gain more information about the structure of interest.

In the mineral exploration industry, the advantages of time-domain airborne EM systems are a greater effective depth of exploration and better lateral resolution compared with frequency-domain systems (Fountain et al., 2005). Christiansen (2006) stated that frequency-domain methods have difficulties penetrating layers with high resistivity in a low-resistivity host rock. However, with TEM methods, this issue is overcome.



In the Cripple Creek Project, due to the advantages of the time-domain systems that provide high penetrating depth and high resolution, it was decided to use an airborne TEM system. A Versatile Transient Electromagnetic System (VTEM) was used over the property. The VTEM system has been developed by Geotech. The system configuration consists of 2-axis (Z-vertical and X-horizontal) induction type ( $dB/dt$ ) EM receiver coils deployed in the middle of the transmitter coil with a cesium magnetometer suspended above it (see Fig. 2.6).

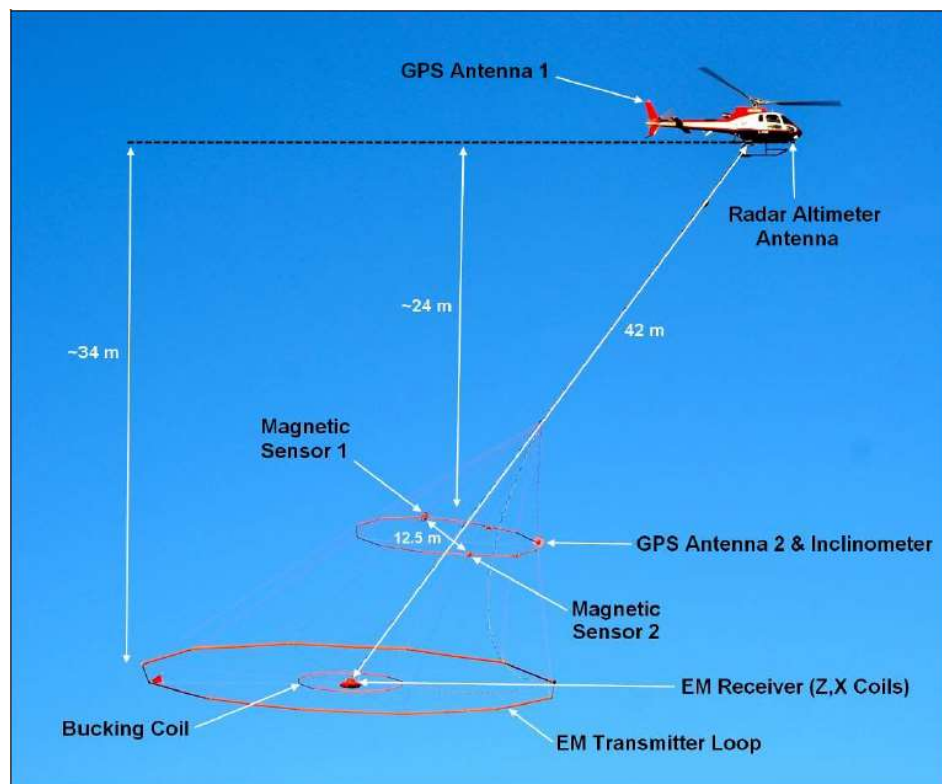


Figure 2.6 VTEM System Configuration. The receiver and the transmitter are at the bottom, and the GPS antenna and the magnetic sensor are at the top (Nahnybida and Willet, 2013).

The VTEM transmitter and receiver coils are in concentric-coplanar, and Z-direction oriented, which is a central loop configuration. The receiver system also includes an X-direction coil to measure the in-line  $dB/dt$  and calculate  $B$ -Field responses. Therefore, VTEM has two receiver coil orientations. The Z-axis coil is oriented parallel to the transmitter coil axis, and both the transmitter coil axis and the Z-axis receiver coil are vertical. The X-axis coil is oriented parallel to the ground and along the line-of-flight. This combined two-coil configuration provides information on the position, depth, dip, and thickness of a conductor.

## 2.3 Frequency-domain EM (FDEM)

Frequency-domain EM is an active EM method with a controlled source like time-domain EM. Transmitter and receiver coils are also used in FDEM. However, in this method, not only the secondary magnetic field is measured, but also, the primary field is measured simultaneously. Because, in FDEM, the primary magnetic field is not turned off at the transmitter loop during the measurement. As given in the TEM method theory, the secondary magnetic field contains information about the electrical properties of the subsurface. Therefore, to remove the effect of the primary field from the response, a bucking coil is used in the systems along with the receiver. It can be expressed that the secondary field measured at the receiver is a complex-valued quantity with the real part called in-phase and the complex part called out-of-phase.

The primary field in the transmitter is a time-harmonic current of the form  $B_p \sin(\omega t)$ . The measured magnetic field in the receiver is then going to be  $B_s \sin(\omega t + \varphi)$  where  $\varphi$  is the phase difference. Therefore, the currents induced in the subsurface will have the same frequency with the primary field. However, they will have a different phase. The total magnetic field in the receiver can be written as (Everett, 2013):

$$\begin{aligned} B_T &= B_p \sin(\omega t) + B_s \sin(\omega t + \varphi) \\ &= B_p \sin(\omega t) + B_s \sin \omega t \cos \varphi + B_s \cos \omega t \sin \varphi \end{aligned}$$

$$= [B_p + B_s \cos \varphi] \sin \omega t + [B_s \sin \varphi] \cos \omega t$$

where  $[B_p + B_s \cos \varphi]$  is called real or in-phase response and  $[B_s \sin \varphi]$  is called quadrature or out-of-phase response. To form a secondary in-phase response, the primary signal is subtracted and  $R_s = [B_s \cos \varphi]$  is acquired.

The Horizontal-Loop Electromagnetic (HLEM) frequency-domain EM method used in this study is a ground-based EM system. This system was used on the Cripple Creek property by Abitibi Geophysics to follow-up on the VTEM anomalies that were observed and to explore the extension of known sulphide mineralization in the area. Fig. 2.7 shows an example of a horizontal-loop EM field application. The HLEM abbreviation will be used in this thesis to refer to the frequency-domain measurement that was made at Cripple Creek.

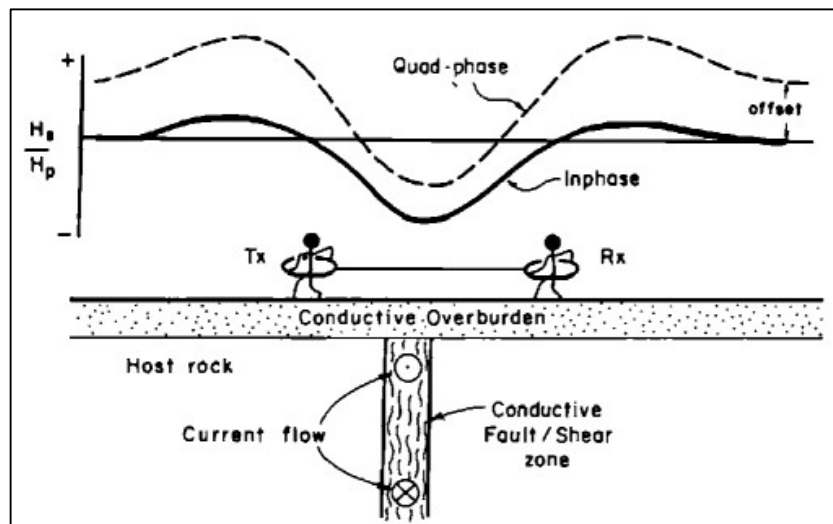


Figure 2.7 A horizontal-loop frequency-domain system and its response over a conductive dike in a less conductive ground with a conductive overburden (McNeill, 1990).

In the frequency-domain method, the transmitter emits a sinusoidally varying current at a specific frequency. For example, in the survey addressed in this research, the measurements were obtained at three different frequencies, 440Hz, 880 Hz, and 1760 Hz. Since the mutual inductance between the transmitter and the conductor is a complex quantity, the electromagnetic force induced in the conductor will be shifted in phase with respect to the primary field. At the receiver, the secondary field generated by the eddy currents in the conductor will also be shifted in phase by the same amount. As mentioned above, the secondary magnetic field can be distinguished from the primary magnetic field using the bucking coil.

In frequency-domain EM, the depth and size of the conductor primarily affect the amplitude of the secondary field. Whether the conductor of interest is highly conductive or not mainly affects the ratio of in-phase to out-of-phase amplitudes: a good conductor gives a higher ratio, and a poorer conductor gives a lower ratio (see Fig. 2.8).

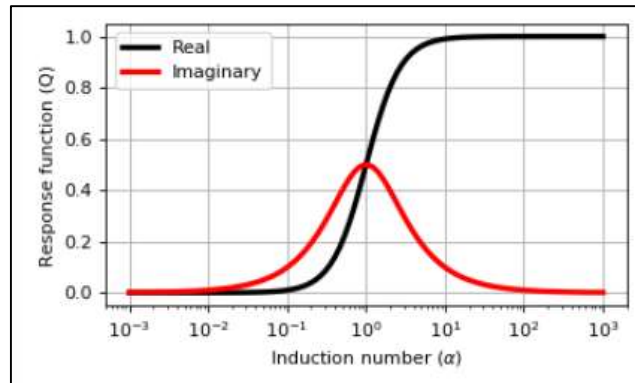


Figure 2.8 The in-phase and out-of-phase responses of a sphere to a frequency-domain system. Adapted from In-phase and out-of-phase response of a sphere, (n.d.).

The calculation and interpretation of FDEM responses are similar to those of the TEM method. Eq. (2.35) can be used for the response at the receiver. Models of conductors like plates and other geometrical shapes are used if further investigation is required.

## **2.4 The Magnetic Method**

In a magnetic survey, the energy source is the Earth's magnetic field, and the physical property of interest is the magnetic susceptibility. Responses are mostly interpreted in terms of geological structures or other features affecting the subsurface distribution of the magnetic susceptibility (Blakely, 1996). Susceptibility is a measure of the ability of a certain material to become magnetized under an external field.

Magnetic materials in the subsurface act like a magnet when they are magnetized. Without an external magnetic field, the Earth's magnetic field here, individual magnetic domains in a magnetic material are oriented in random directions, and the net magnetic field is zero. When they are placed in an external magnetic field, the magnetic domains direct toward the direction of that external field, resulting in the magnetization of the material.

Magnetized materials create a magnetic field. In the geophysical surveys, this generated magnetic field is measured, and from it, one attempts to obtain the distribution of the susceptibility in the subsurface.

Magnetization is an important quantity of interest in mineral exploration. The significant equations for magnetic surveys are the following:

$$\mathbf{B} = \mu \mathbf{H}, \quad (2.36)$$

$$\mu = \mu_0(1 + \kappa), \quad (2.37)$$

$$\mathbf{M} = \kappa \mathbf{H} + \mathbf{M}_{NRM}, \quad (2.38)$$

$$\mathbf{H} = \frac{1}{\mu_0} (\mathbf{B}_0 + \mathbf{B}_A). \quad (2.39)$$

In the above equations,  $\mathbf{M}$  is the magnetization,  $\mathbf{B}_0$  is the external or inducing field, in this case, the Earth's field,  $\mathbf{B}_A$  is the anomalous local field,  $\mathbf{M}_{NRM}$  is the Natural Remanent Magnetization that describes the ability of matter to maintain a remanent magnetization without external field, and  $\mu_0$  is the magnetic permeability in free space ( $4\pi \times 10^{-7} \text{ H/m}$ ). Finally,  $\mathbf{H}$  and  $\kappa$  are the magnetic field intensity and susceptibility, respectively.  $\mathbf{H}$  and  $\mathbf{M}$  have units of Amperes per meter (A/m), and  $\kappa$  is dimensionless.  $\mathbf{B}$  has units of Tesla (T).

As presented, Eq. (2.38), the magnetization within a magnetic material is proportional to the magnetic field intensity and susceptibility at that location. That means the more susceptible a material, the more magnetized it becomes. The susceptibility values of common minerals and rocks are given in Figure 2.10.



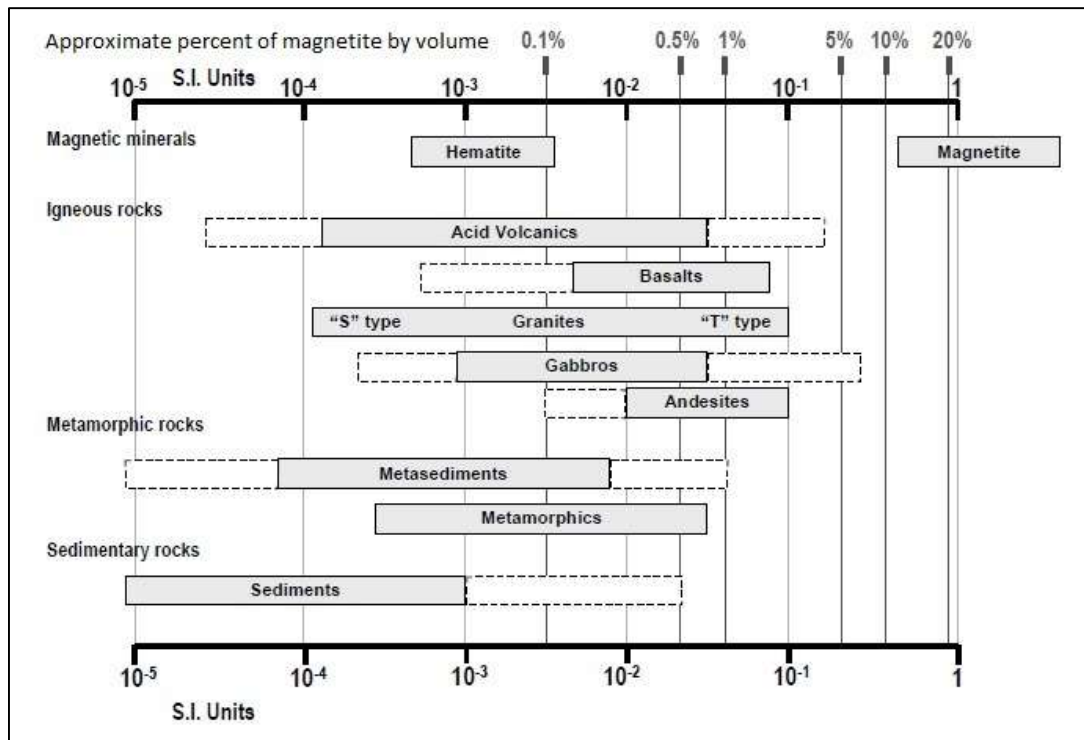


Figure 2.9 Magnetic susceptibilities for common mineral and rock types (adapted from Clark and Emerson 1991).

The total magnetization of a rock, which is a vector quantity, includes two components that are induced and remanent. Induced magnetization depends on the external field (Clark and Emerson, 1991). A single or several components of the total induced field resulting from susceptible materials in the subsurface can be measured. In most cases, the measurements are the magnitude of the total field instead of the individual components.

The relation between the measured magnetic field and rock magnetization is given as (Basic Principles of Magnetism, 2017):

$$\mathbf{B}^{obs}(r) = \frac{\mu_0}{4\pi} \int_v \nabla \nabla \frac{1}{r} \cdot \mathbf{M} dV, \quad (2.40)$$

where  $B^{obs}(r)$  is the observed magnetic field at the distance  $r$  from the magnetic material with magnetization  $M$ . In general, the magnetic data consist of Total Magnetic Intensity (TMI) measurements that are given by

$$B^{TMI} = |\mathbf{B}_0 + \mathbf{B}_A|. \quad (2.41)$$

We measure the magnitude of the field rather than the individual components. Mostly, we are interested in the local anomalous field in magnetic data. That is why only the local anomalous field is used for inversion to give a model of the susceptibility in the subsurface. Therefore, the Total Magnetic field Anomaly is given by:

$$B^{TMA} = |\mathbf{B}_0 + \mathbf{B}_A| - |\mathbf{B}_0|. \quad (2.42)$$

### **3 Modelling of Geophysical Data**

Any geophysical exploration is conducted in order to gather information about the subsurface to find a target of interest based on its physical properties. In some cases, the observed data may be interpreted directly using shaped shapes or some imaging techniques that are explained in Section 3.3 to make out the general characteristics of the target of interest. But further studies are often necessary, which is where forward modelling and inversion come in.

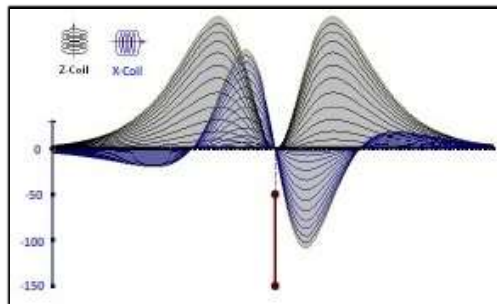
#### **3.1 Plate-modelling of EM Data**

In this research, we have roughly interpreted the observed TEM data at first by using anomaly shapes like peaks and troughs. Then, we have compared this with the observed horizontal-loop frequency-domain EM (HLEM) responses. After that, we have modelled possible plate-like structures in the area of interest. This kind of modelling is a simple but fast approach to take a look at anomalies in large airborne data-sets to determine the discrete structures in the subsurface. A series of common models was taken from the Geotech Report (2012) for the purpose of gaining a general understanding of the responses generated by thin, plate-like conductors of different orientations in a resistive halfspace (see Fig. 3.1). The responses were calculated using the Maxwell modelling program (see EMIT 2016 in references).

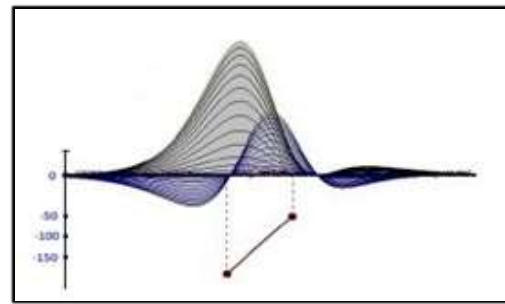
The program Maxwell is often used for simple plates in free space in order to model resistive halfspace. Therefore, to get better results, it can be said

the program Maxwell is only good for modelling of simple plate-like conductors. This can be addressed as a disadvantage, but it is a fast and usable approach for plate-like conductors like faults, dikes, or plate-like discrete mineral deposits.

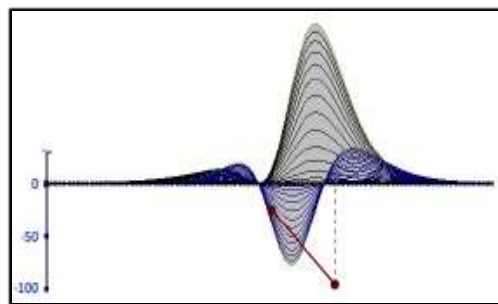
After fast interpretation for the discrete target of interest thought to be the mineralization zone, further investigations were pursued. Program EM1DTM was used to invert the airborne data to effectively get a pseudo-3D model for interpretation in detail.



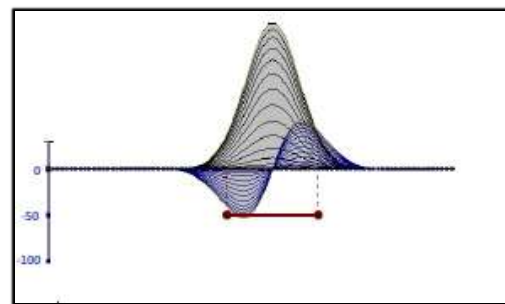
Vertical thin plate



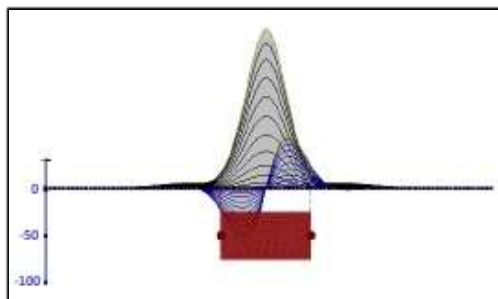
Inclined thin plate leaning left side



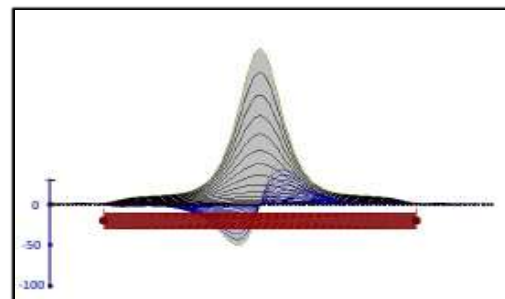
Inclined thin plate leaning right side



Horizontal thin plate



Horizontal thick plate



Horizontal thick plate

Figure 3.1 TEM responses over different plate-like conductors. The grey curves are the z-component of the response. The blue curves are the x-component of the response. (Adapted from Geotech Ltd. Report, 2012.)

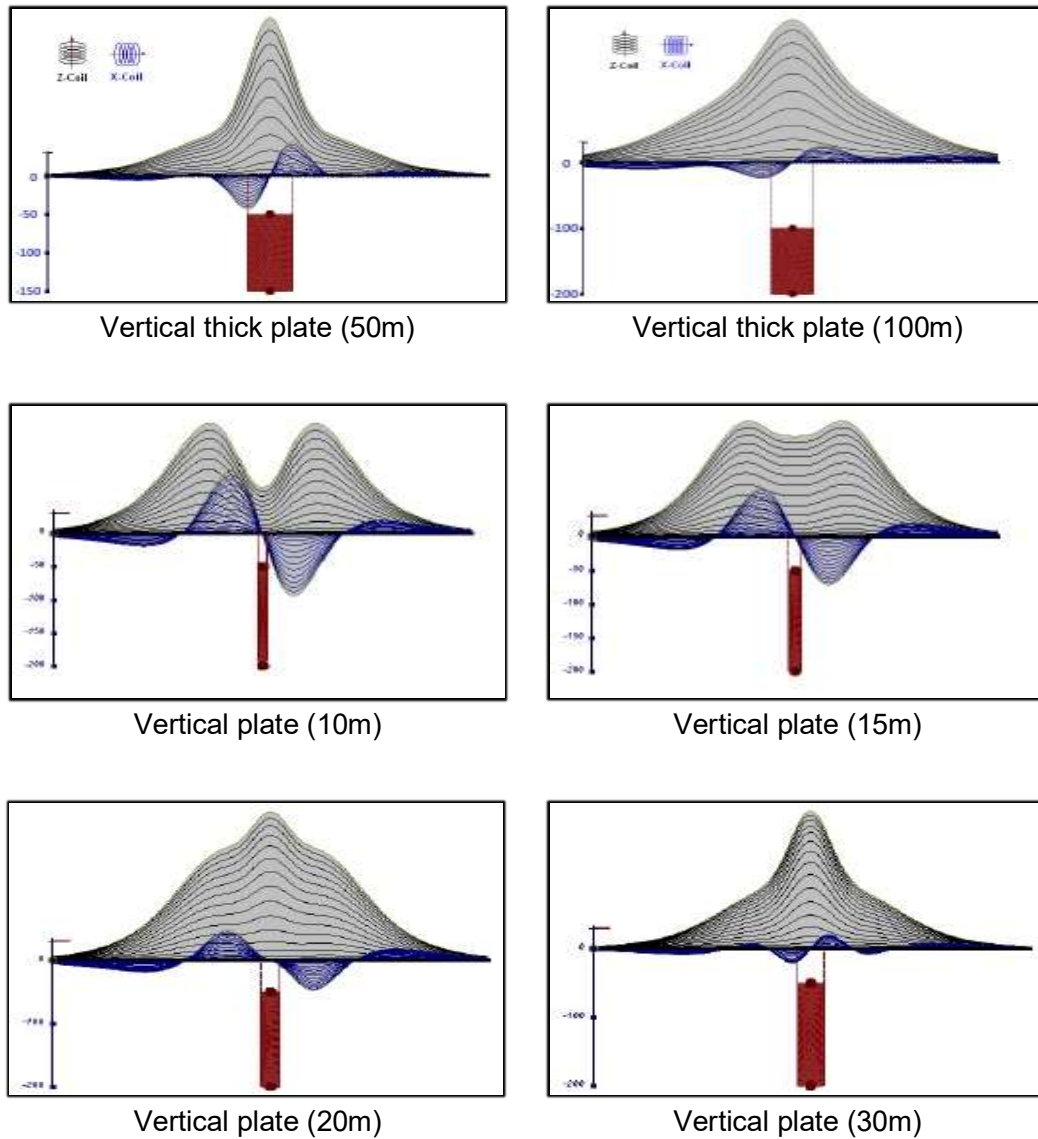


Figure 3.2 TEM responses over different plate-like conductors. The grey curves are the z-component of the response. The blue curves are the x-component of the response. (Adapted from Geotech Ltd. Report, 2012.)

### 3.2 Inversion of Geophysical Data

The goal of the inversion is to build a model that fits the observations, that is, the real geophysical data obtained from a field survey, within a reasonable error. This is realized by formulating inversion as an optimization problem. Therefore, the Earth model is sought that minimizes the objective function:

$$\Phi = \phi_d + \beta \phi_m. \quad (3.1)$$

Forward modelling is the calculation of responses for a model of the subsurface physical property distribution, which might be 1D, 2D, or 3D. That is, before the inversion process, predicted data are calculated from an initial or hypothesized model,  $m$ , using forward modelling algorithms.

In an inversion process, the forward modelling is used to calculate the data for a physical property model, and the misfit between the predicted and the observed data is calculated. In Eq. (3.2),  $\phi_d$  is the typical sum-of-squares measure of the data misfit:

$$\phi_d = \|W_d(d - d^{obs})\|^2, \quad (3.2)$$

where  $\|\cdot\|^2$  indicates the  $l_2$ -norm,  $d^{obs}$  is the vector containing the  $N$  observations, and  $d$  is the vector of forward-modeled data. The matrix  $W_d$  contains the estimated noise in the observations. It is required for the calculations because

$d^{obs}$  always contains a certain amount of noise in practice, and the inclusion of this matrix allows the inversion to take into account the noise in the data.

It is assumed that the noise in the observations is uncorrelated; that is, the noise in each observation point is independent.  $s_0$  is a scale factor that specifies the average size of the noise while  $\hat{s}_i$  shows the amount of noise in the  $i$ th observation relative to that in the others. Therefore, the matrix  $W_d$  in Eq. 3.2 can be written as

$$W_d = diag \left\{ 1/(s_0 \hat{s}_1), \dots, 1/(s_0 \hat{s}_N) \right\}. \quad (3.3)$$

The model-structure component of the objective function is  $\phi_m$ :

$$\phi_m = \|W_s(m - m_s^{ref})\|^2 + \|W_r(m - m_r^{ref})\|^2, \quad (3.4)$$

where  $m$  is the vector containing the model parameters,  $m_s^{ref}$  and  $m_r^{ref}$  are the reference models of the smallest and the flattest (or smoothest) terms constructed with prior information.  $W_s$  and  $W_r$  are the smallest and the flattest model weighing matrices.  $W_s$  is used to make the constructed model close to the reference model, and  $W_r$  is used to calculate the differences between the model parameters in neighbouring the cells/layers, and hence to calculate a measure of how rough the model is.

There are numerous functions that can be used as a measure of the length of a vector. The general measures of the length of a vector like Huber's M-measure



are used during inversion. Detailed information about the use of general measures in non-linear inverse problems is given by Farquharson and Oldenburg (1998).

Geophysical inverse problems are inherently non-unique, which means that there are many different solutions under the desired data misfit. This unsatisfying problem is solved by adding prior information to the inverse problem to find a meaningful model, in this case, adding constraints and regularization. In Eq. (3.1),  $\beta$  is the regularization or trade-off parameter that balances the minimization of the misfit and minimization of the amount of structure in the model. The details are presented in Oldenburg and Li (2005).

After successively trying different models, each of which is hoped to be an improvement over the preceding one, the inversion program gives us the best model that fits the observed data with the aimed-for data misfit value. These tries are called iterations, and the process is called iterative inversion. Iterative inversion is required for the solution of the non-linear problems. Although EM inversion is non-linear, magnetic inversion is linear due to Eq. 2.40, the observed magnetic field. Looking at Eq. 2.40, the observed magnetic field is linearly proportional to the magnetization in the subsurface. However, looking at Section 2, EM field functions are non-linear. Therefore, EM inversion needs an iterative process. In an iterative process, sensitivity matrices are used, which are partial

derivatives of the data with respect to the model parameters (Farquharson, 1996).

If we have a reasonable fit to the observations, the final models for all measurement locations are visualized in Paraview, and the 3D model or image assessed to try to figure out whether there are artefacts or not in the constructed model. If something is wrong, the inversion process is repeated with different parameters. Otherwise, it is assumed that the results are reasonable to use for geological interpretation.

### **3.3 1D TEM Inversion**

Because of the complexity of electromagnetic methods, TEM data-sets have been interpreted using fast and simple techniques like plate-modelling (see Section 3.1) or other techniques such as time constant analysis (e.g. Holladay 2006), apparent conductivity, conductivity depth imaging/transform (CDI/CDT) (e.g. Fullagar 1989; Macnae 1991). These interpretation techniques are not expensive, but the results are not consistent with conductivity values measured for targets in general. In a parametric inversion, a non-linear problem is solved to find the thicknesses and conductivities of a limited number of layers. This technique has the potential to generate a logical representation of the Earth. However, one of the setbacks of this technique is that the results depend on the assumed number of layers and the starting model used in the iterative inversion (Farquharson and Oldenburg, 1993).

It might seem more natural to solve 2D and 3D problems to show the subsurface; however, the computational complexity of the EM inverse problem increases dramatically in higher dimensions, and this is the primary reason for the slow inversion process (Oldenburg, 1990). Otherwise, obviously, it is inevitable that geological noise is present when describing a 3D world by a 1D model. Yang (2014) has shown that even though using 2D or 3D inversion is better for fields that consist of complex geological structures, sometimes using 1D inversion can be enough, especially for good-isolated conductors and horizontal structures or

layered models such as plate-like or largely mineralization deposits and faults. Also, 1D inversion can reasonably be used for a large data-set, especially airborne, to reduce computational time.

In the data acquisition of a TEM experiment, a step or ramp turn-off current flowing in a transmitter loop induces currents in the Earth, and the time decay of the vertical component of the induced magnetic field, or its time derivative, resulting from these induced currents is measured as a function of time (Farquharson and Oldenburg, 1993). These measurements can be at any point on the surface of the Earth or at any point beneath the airborne system used in the survey.

In order to reproduce a potentially more accurate model compared to the relatively simpler methods above while still being computationally feasible for an airborne survey, a one-dimensional (1D) layered model is used (see Fig. 3.3 and 3.4). The parameters of the horizontally layered conductivity model of the Earth are adjusted by the inversion, keeping fixed thicknesses of the layers, until the best fit is achieved between the calculated model and observed data (see Section 3.2).

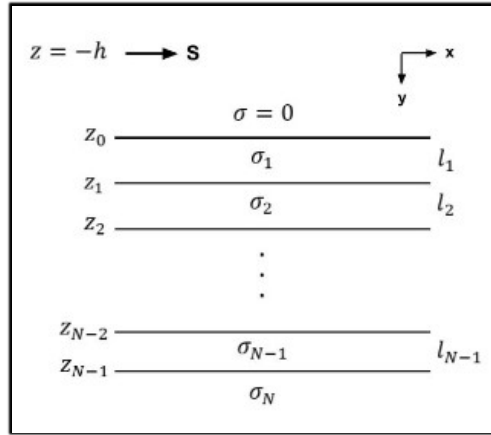


Figure 3.3 The horizontally layered conductivity model of the Earth.  $z_j$  is the depth of the bottom of the  $j$ th layer,  $\sigma_j$  and  $l_j$  are the conductivity and thickness of the layers, respectively.  $S$  represents the source. (Modified from Farquharson and Oldenburg, 1993.)

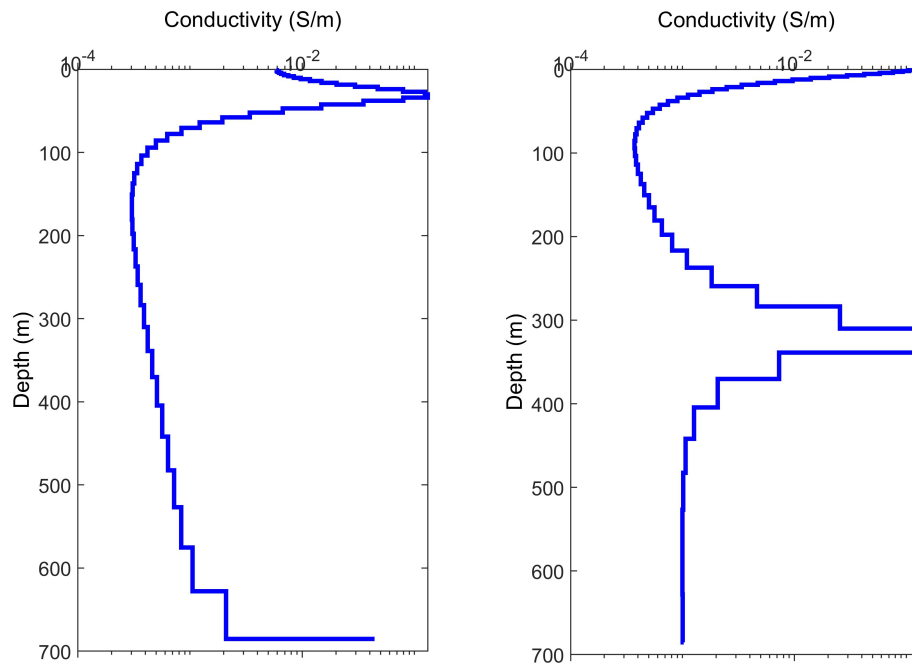


Figure 3.4 Two examples of inversion results of TEM soundings from the Cripple Creek data-set (Line 2290, 15<sup>th</sup> and 60<sup>th</sup> soundings).

1D models recovered from the inversion are concatenated and interpolated to form a 3D volume of conductivity, which is then viewed in Paraview. Farquharson et al. (2003) is an example of this type of research.

### **3.4 Inversion codes used**

#### **3.4.1 1D TEM Inversion Code – EM1DTM**

Firstly, EM1DTM stands for electromagnetic (EM), one-dimensional (1D), time-domain observations (T), and magnetic source or receiver (M). It was developed by the University of British Columbia's Geophysical Inversion Facility. The mathematical background is outlined in Farquharson and Oldenburg (1993).

The code EM1DTM performs 1D inversion for TEM data for a horizontally layered Earth, both separately for one sounding and for multiple soundings. It is designed to provide options for using the magnetic field, or its time derivative, or both. The transmitter current waveform can be a step-off, a linear ramp turn-off, or a general discretized waveform. The transmitter and receiver or receivers can be on the ground or in the air. For more information, time-domain electromagnetic methods are presented in Section 2.

For the 1D model of the Earth, as shown in Fig. 3.1, fifty uniform horizontal layers are considered, and their conductivities are determined. The thicknesses of the layers in a model increase by a factor of 1.5. The magnetic susceptibilities of the layers are assumed to be the same as that of free space.

For forward modelling, the magnetic field for a particular source and receiver is calculated in the frequency domain, and the time-domain values of the magnetic field calculated by Fourier transform. The computational details are described in

Farquharson and Oldenburg (1993), Farquharson and Oldenburg (1996), and Farquharson et al. (2003).

There are four different inversion algorithms within program EM1DTM. The choice of the inversion algorithm is significant because it can affect the resulting model. The algorithms determine the trade-off parameter  $\beta$  automatically, or it is selected manually by the user. These algorithms are user-supplied cooling schedule, discrepancy principle, generalized cross-validation (GCV), and L-curve criterion. The details are presented in Farquharson and Oldenburg (2004).

The components of the objective function (Eq. 3.1) used in EM1DTM are the same as given in Eq. 3.2.

It is assumed that the noise in the observations is uncorrelated; that is, the noise in each observation point is independent. The average size of the noise is given in Eq. (3.3). The model structure components of the objective function are  $\phi_m$ :

$$\phi_m = a_s M_m^s \|W_s(m - m_s^{ref})\| + a_z M_m^z \|W_z(m - m_z^{ref})\|, \quad (3.5)$$

where  $m$  is the vector comprising the logarithms of the layer conductivities, and  $M_m^s(x)$  and  $M_m^z(x)$  are measures of a length of the vector  $x$  as described above. The matrix is:

$$W_s = \text{diag}\{\sqrt{t_1}, \dots, \sqrt{t_{M-1}}, \sqrt{t_M}\}, \quad (3.6)$$

where  $t$  is the layer thickness of the  $M$  layer. The matrix  $W_z$  is:



$$W_z = \begin{pmatrix} -\sqrt{\frac{2}{t_1 + t_2}} & \sqrt{\frac{2}{t_1 + t_2}} & & & \\ & -\sqrt{\frac{2}{t_2 + t_3}} & \sqrt{\frac{2}{t_2 + t_3}} & & \\ & & \ddots & & \\ & & & -\sqrt{\frac{2}{t_{M-1}}} & \sqrt{\frac{2}{t_{M-1}}} \\ & & & & 0 \end{pmatrix} \quad (3.7)$$

The vectors  $m_s^{ref}$  and  $m_z^{ref}$  contain the layer conductivities for the two possible reference models. Therefore, the two terms in the objective function, Eq. (3.5), are called “smallest” and “flattest” components. The coefficients  $a_s$  and  $a_z$  govern the importance of these two terms. Lastly,  $\beta$  is the trade-off parameter, briefly mentioned in Section 3.2, that balances the minimizing of the misfit and minimizing the amount of the model structure, i.e., it controls the relative importance of the model smoothness.

For the TEM inversion in this study, a trial and error process was carried out to select the best algorithm for the data-set. The best results were obtained from the user-supplied cooling schedule. The first iteration is started from a  $\beta$  value of 1000. This value is halved at each iteration until 10 is reached, then the inversion continues with the value of 10 until it reaches the pre-determined maximum number of iterations. These choices were found to give the most consistent results.

To plot a 3D composite model of the 1D inversion results for better interpretation, a subprogram EM1D3D was used to generate a 3D rectilinear mesh under the observation points for the whole survey. Ultimately, the 3D picture of the area of interest was visualized in Paraview, which is an open-source application for interactive, scientific visualization.

### 3.4.2 3D Magnetic Inversion code – VIDI

Firstly, VIDI stands for Voxellized Discretization written by Dr. Peter Lelièvre. It is a mesh-based inversion program that determines the physical property values or lithologies inside the mesh cells. The region of interest in the subsurface is discretized into many volumetric cells with constant susceptibility (see Fig. 3.5). For a rectilinear mesh, magnetic anomalies measured, which are described theoretically in Section 2.4, are calculated on cell faces and then are interpolated to the cell centres

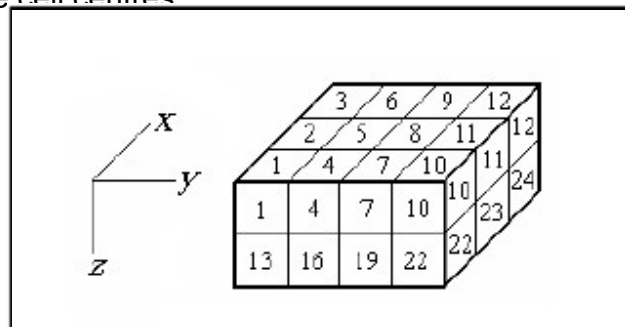


Figure 3.5 Rectilinear mesh example. The area of interest under the observation points is discretized using a rectilinear mesh. (Modified from Lelièvre, 2003).

Two different inversion approaches are available. One is the general inversion that assumes the model values as physical property values which is used in this study. The other one is the lithological inversion that can be designed for specific rock types whose physical properties are known or assumed.

The program supports five different data types: vertical component gravity, gradiometry gravity, total magnetic field, magnetic amplitude, and first-arrival seismic travel times. In this study, total magnetic field data were inverted to give a susceptibility model. The critical point about total magnetic field data-sets is that the geomagnetic field at the time of the survey needs to be subtracted from the data-set because the program uses only regional anomalies to calculate susceptibilities.

A similar inversion algorithm is used in program VID1 as with EM1DTM as given in Section 3.2. However, the magnetic inversion is a linear inverse problem, whereas the EM inversion is a non-linear inverse problem. It requires a reference model and an initial value of the trade-off parameter. Regularization includes traditional smallness and smoothness measures. Contrary to EM1DTM, in program VID1, the smoothness axes can be rotated to any arbitrary orientation, and the lambda trade-off parameter is used instead of beta. The contrast between these two trade-off parameters is that lambda is used as a multiplier before the data misfit term instead of the structure term (see Eq. 3.1).

In the solution of the non-linear inverse problem, the measure of the data misfit and model structures are required. There are three different options for these general measures in the program VIDI that are standard  $l_2 - norm$ , Ekblom, and Huber measures. In this study, we obtained better results from the Ekblom measure. The details of the use of these measures are outlined in Farquharson and Oldenburg (1998).

The relationship between the cells and the observation points is crucial for magnetic inversion, as for other potential-field data inversions, due to fundamental non-uniqueness in inversions of potential-field data. Any magnetic data can be fitted either with smaller susceptibility values near the surface or with larger susceptibility values at depth (Lelièvre 2003). In program VIDI, there are three different weighting options to overcome this issue, namely, depth, distance, and sensitivity weightings (as well as the option to include no weighting). If no weighting is used, it must be accepted that all the magnetic anomalies result from near-surface sources for near-surface investigations.

The depth weighting for the  $j^{th}$  cell is:

$$w_j = (d_j + h_0)^{-wpower}, \quad (3.8)$$

where  $d_j$  is the depth of the cell centroid, and  $h_0$  is the average height of the survey.

The distance weighting for the  $j^{th}$  cell is:

$$w_j = \left( \sum_{i=1}^N |r_i + wzero|^{(wpower*wnorm)} \right)^{(wbeta/wnorm)}, \quad (3.9)$$

where the sum is over all the observations, and  $r_i$  is the distance between the cell centroid and the  $i^{th}$  observation location.  $wzero$  is half of the smallest cell dimension.  $wbeta$  and  $wnorm$  are the parameters to control the weightings prior to inversion.

The sensitivity weighting for the  $j^{th}$  cell is:

$$w_j = \left( \frac{1}{2} \sum_{i=1}^N \left| \frac{G_{ia}}{v_a} \right|^{(wnorm)} + \frac{1}{2} \sum_{i=1}^N \left| \frac{G_{ib}}{v_b} \right|^{(wnorm)} \right)^{(wbeta/wnorm)}, \quad (3.10)$$

where the sum is over all the observations,  $G_{ij}$  is an element in the sensitivity matrix and  $v_j$  is the volume of the cells.

Different weighting options can be taken advantage of depending on the topography of the survey area. Because depth weightings are determining the relationship between the mesh and the observation points.

## **4 Survey Area**

The Cripple Creek property is in the north of Newfoundland, Canada, and is located approximately 21 kilometres north of the Gander area (see Fig. 4.1). The topography is slightly rugged with elevation changing from 10 to 130 m above sea level.

Exploration work in the area dates back to the investigation of chromite deposits in the 1930s. During this work, three chromite deposits were found in the Gander River complex, which is an ophiolite, including the core area, which is studied in this research.

In the following years, numerous gold mineralization discoveries have been found in the whole project area and the surroundings. Nahnybida and Willett (2013) describe in detail the previous work done in the entire region.

The significant Au value in the whole Cripple Creek property that is up to 19 g/t Au is associated with up to 15.5% Cu and Zn. According to previous work, the main mineralization in the area is possibly a VMS (Volcanogenic Massive Sulphide) deposit, which might include Au, Cu, Zn, and Ag.

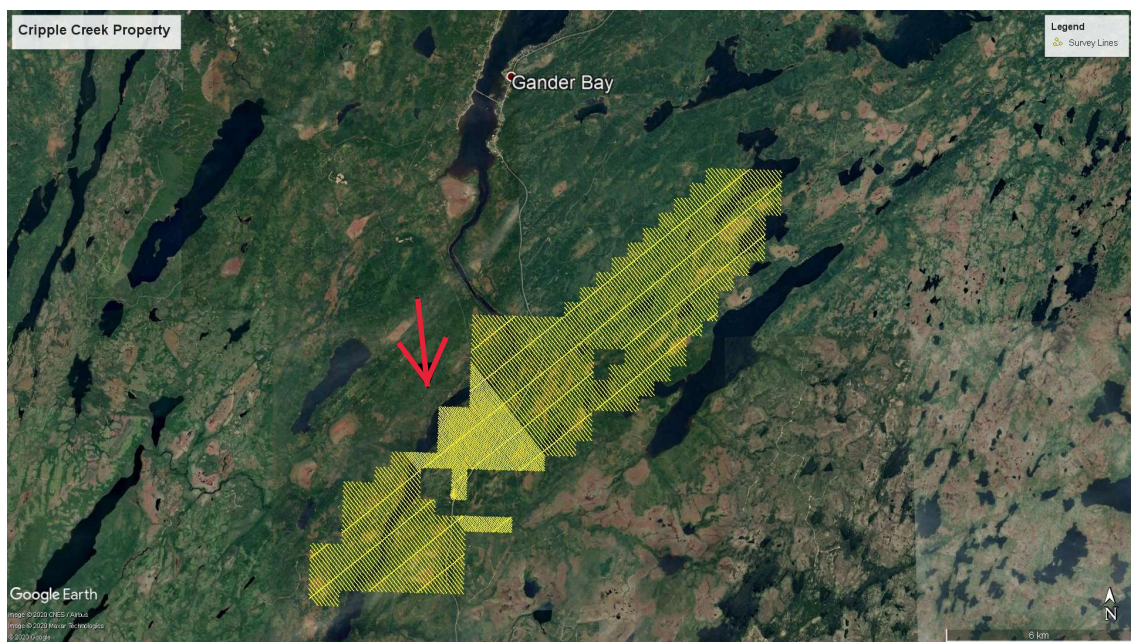
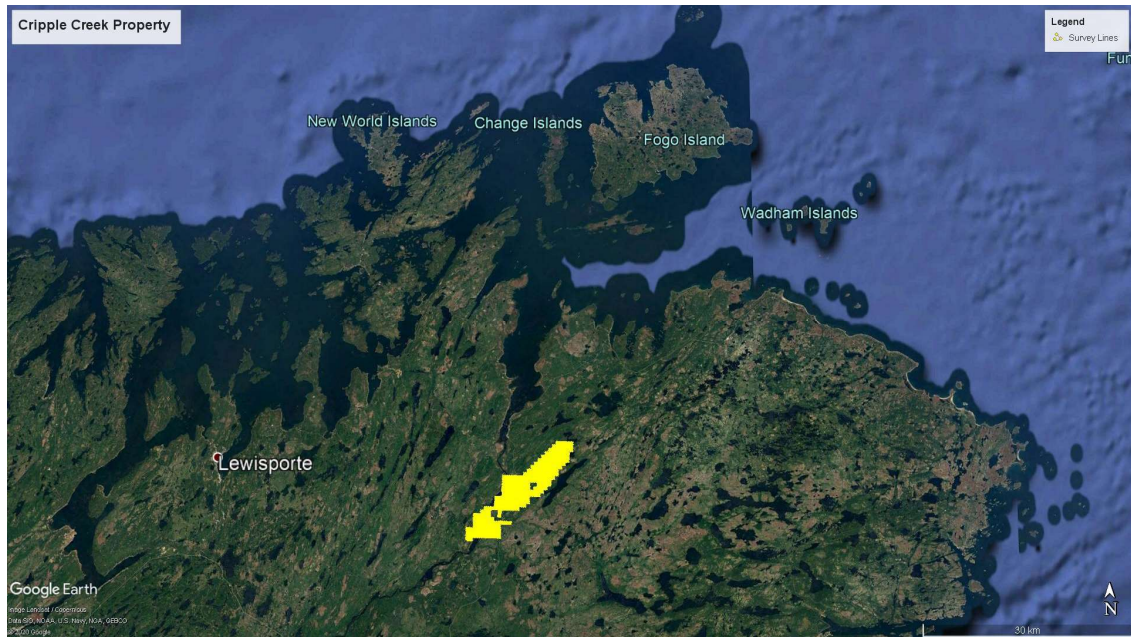


Figure 4.1 The location of the Cripple Creek Property and Survey Lines. The red arrow shows the area of interest. (Retrieved from Google Earth.)



## 4.1 Geology

The Cripple Creek property covers two tectonostratigraphic zones, the Dunnage Zone and the Gander Zone (see Fig. 4.1 and 4.2). The Gander River Complex is the boundary formation between these two zones, an ophiolite comprising ultramafic to felsic plutonic rocks and mafic volcanic rocks.

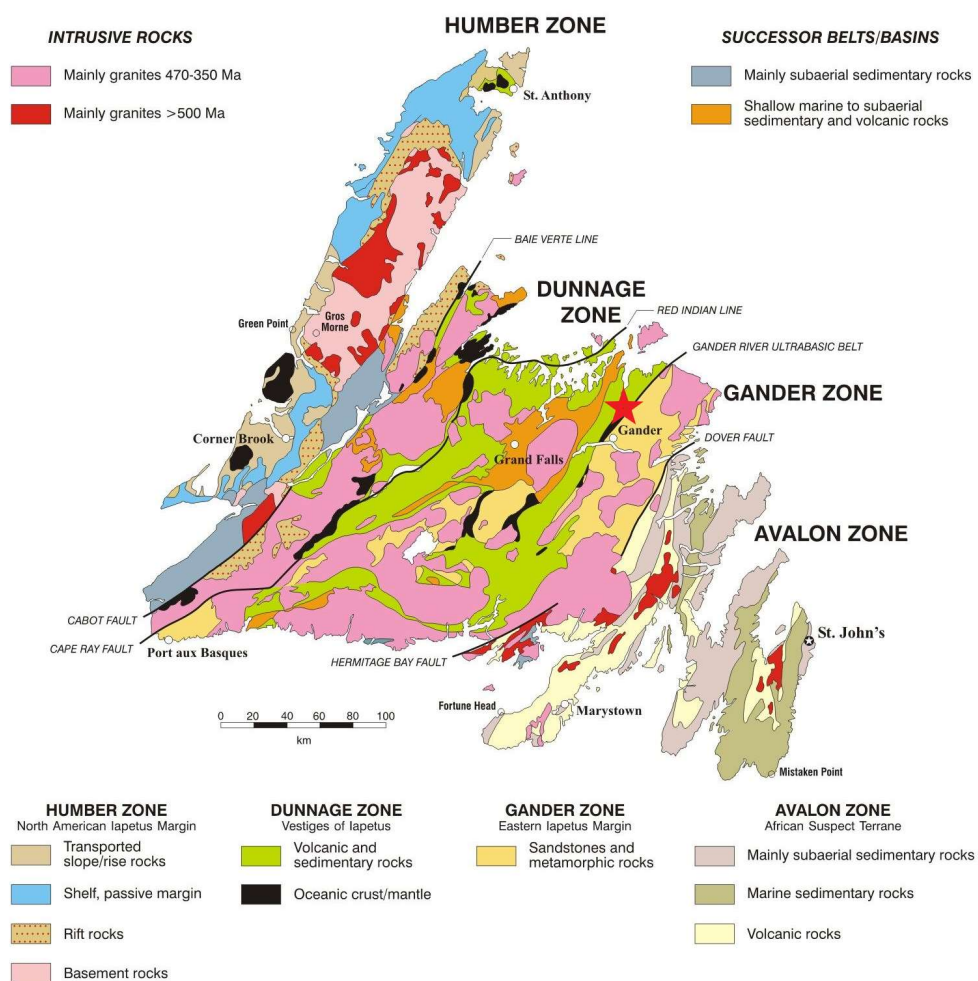


Figure 4.2 Geology Map of Newfoundland and the location of the Cripple Creek Property shown by the red star (<https://www.gov.nl.ca/iet/files/mines-maps-nf.pdf>).



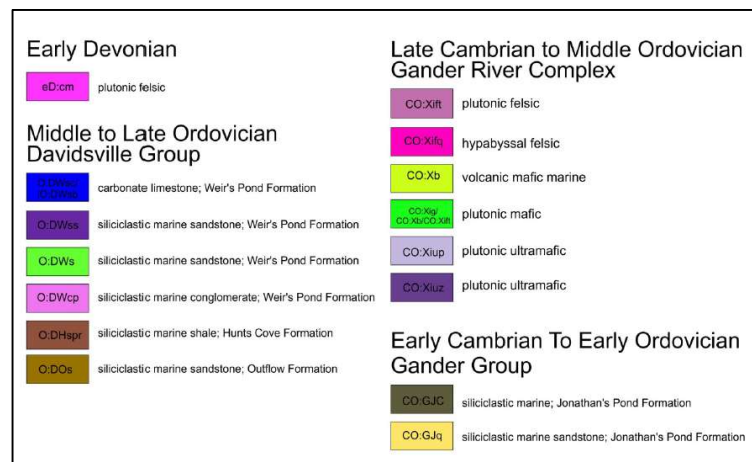
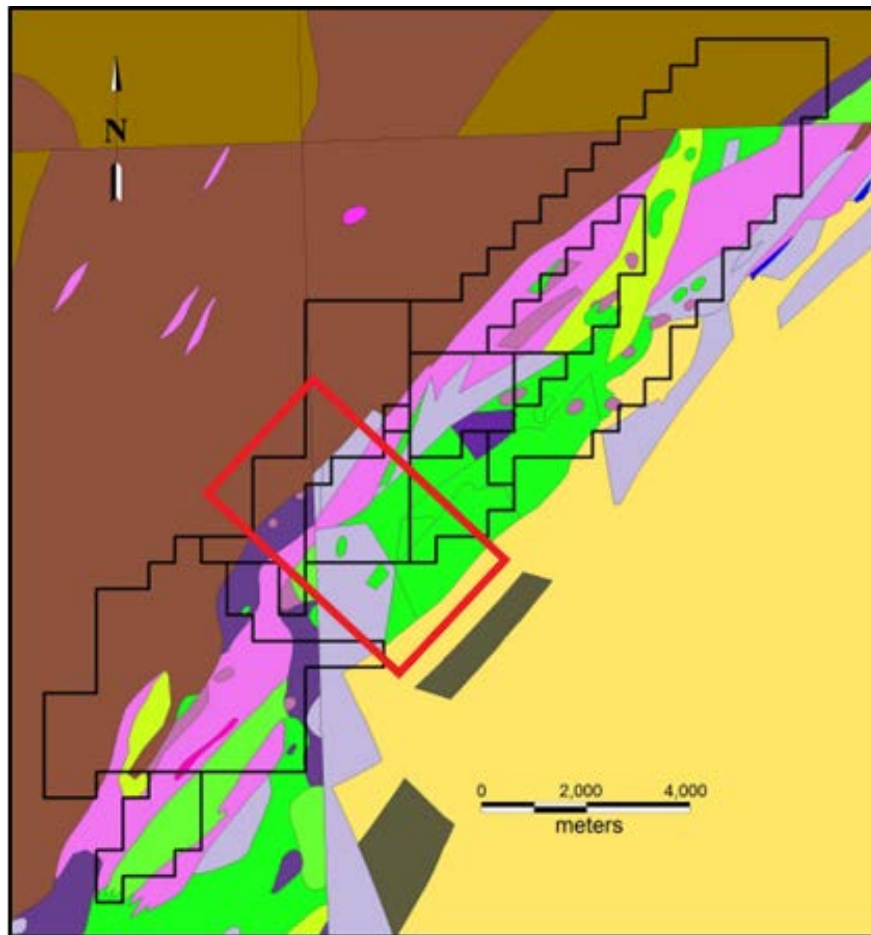


Figure 4.3 Regional geology of the Cripple Creek property. The red rectangle is the Core Area. (Adapted from Nahnybida and Willett, 2013.)



greenschist facies. The Gander Group has been metamorphosed from greenschist to amphibolite facies. The Cripple Creek claims are underlain almost entirely by rocks of the Davidsville Group and Gander River Complex, with Gander Group rocks restricted to a northeast-trending belt of Jonathan's Pond Formation sandstone along the northwestern shore of Weir's Pond (see Fig. 4.3).

## **4.2 Mineralization**

The main mineralization type in the area is VMS, which stands for Volcanogenic Massive Sulphide. This mineralization occurs as lenses of massive polymetallic sulphide that form at or near the seafloor in submarine volcanic environments (Galley et al., 2007). These kinds of mineralization deposits actively form on the seafloor all over the world as modern VMS deposits and have been formed throughout geological time, forming ancient VMS deposits. They occur where metal-enriched fluids from the oceanic crust meet cold ocean water, causing the metals to be deposited (see Fig. 4.5).

These types of mineralization are encountered at both mid-ocean ridges where plates pull apart and subduction zones where plates converge together. The hydrothermal circulation in the seafloor environment causes interaction between seawater and hot crustal rocks. And this interaction then leads to the forming of VMS deposits (see Fig. 4.5 and Fig. 4.6.)

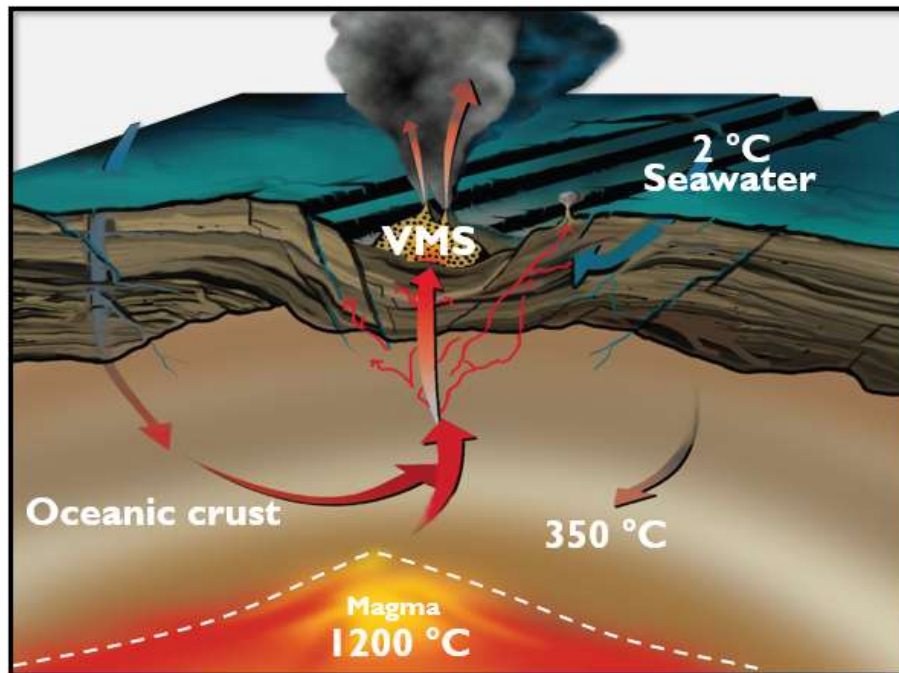


Figure 4.5 Typical VMS occurrence at mid-ocean ridge (from Dr. Andrews, personal communication).

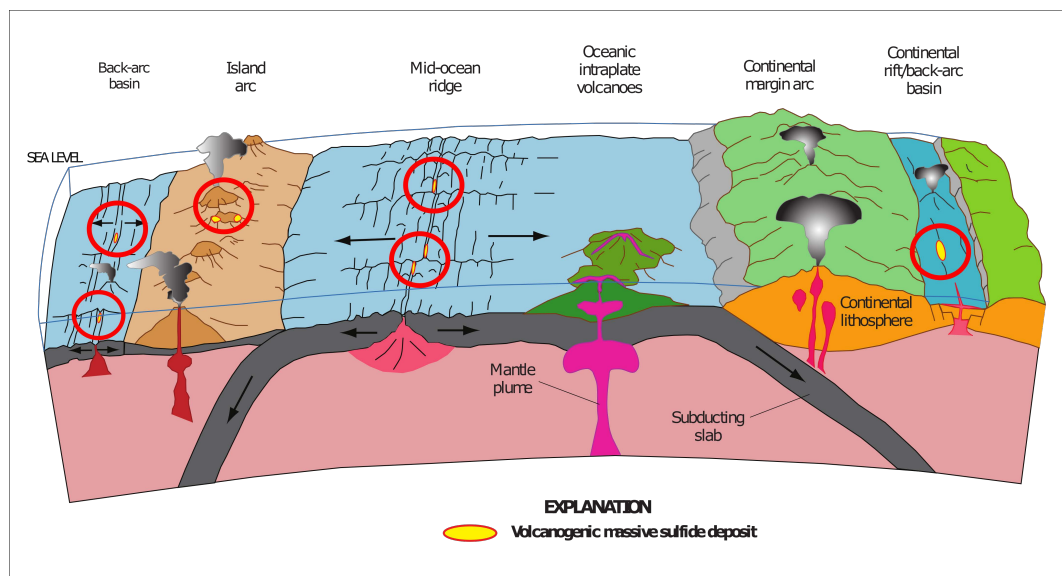


Figure 4.6 VMS deposit occurrence models in different structures (modified from Shanks and Thurston, 2010).

This seafloor hydrothermal convection near the volcanic environment form VMS deposits. Their host rocks can be either volcanic or sedimentary. The VMS deposits are major sources of Zn, Cu, Pb, Ag, and Au, and significant resources for Co, Sn, Se, Mn, Cd, In, Bi, Te, Ga, and Ge. Some also include As, Sb, and Hg. They make up 27% of Canada's Cu production, 49% of its Zn, 20% of its Pb, 40% of its Ag, and %3 of its Au (Galley et al., 2007).

VMS deposits are seen in seafloor environments worldwide while it is seen in different places as ancient deposits such as Newfoundland and Labrador (see Fig. 4.6 for ancient VMS deposits).

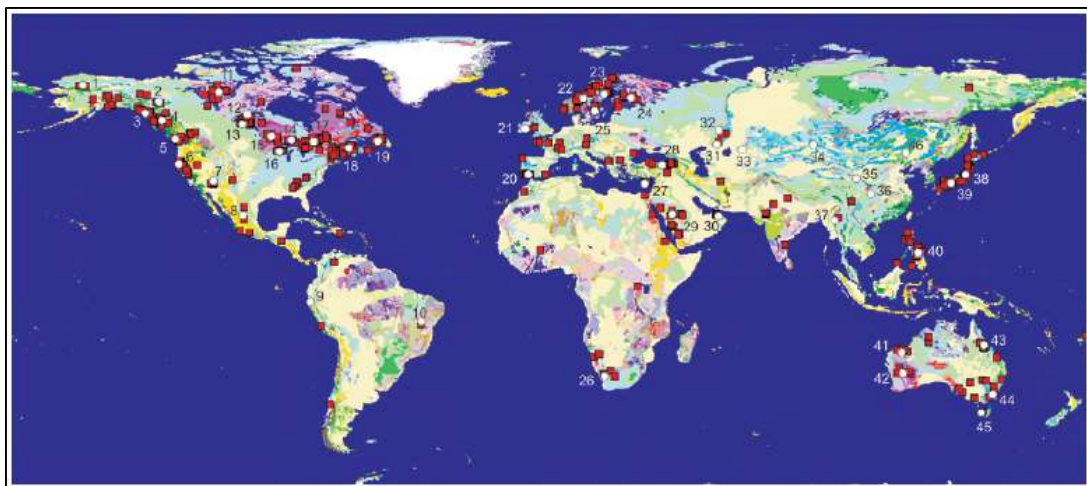


Figure 4.7 Geographical distribution of ancient VMS deposits (Galley et al., 2007).

### 4.3 Previous Works

The Cripple Creek area has been explored since the 1930s. The first exploration was for a chromite deposit. Nahnybida and Willett (2013) and Willett

(2014) give the details about previous work done in the area on geological, geochemical, and diamond drilling.

As for geophysical surveys, an airborne EM-magnetometer survey addressed in this study was carried out in 2012, and IP surveys have been conducted over most of the property since 1973. In 1988, Gander River Minerals completed soil sampling and IP an survey over a 6.5 km-long grid located over Cripple Creek Grid, Weir's Brook, and Muddy Gallies (see Fig. 4.6). The best assay was 2.84 g/ton over 0.9m (Sheppard, 1989 as cited in Nahnybida and Willett, 2013). The Core area, which is the area of interest in this research, is located on the Cripple Creek grid that is shown in Fig. 4.4. A hole drilled on the Cripple Creek grid targeting two IP anomalies to the north of the Cripple Creek prospect intersected heavily pyritized diabase and graphitic sediments. Gander River Minerals also drilled 2 holes in the Muddy Gullies area, targeting IP anomalies; they concluded that graphitic sediments were responsible for the chargeability response (Strickland et al., 1991, as cited in Nahnybida and Willett, 2013).

In 2006, Richmond Mines drilled 7 holes to test the Cripple Hand, a mineralization in the Cripple Creek property, which Richmond interpreted to be coincident with a 1 km long NE-SW IP chargeability trend. The best assay result from drilling was 2.07 g/t Au over 0.5m in hole CC-05-06, and the best copper intercept of 0.27% over 0.5m from drilling in the area; all other drill results returned only weakly anomalous gold and copper values at best

(Pilgrim, 2006 as cited in Nahnybida and Willett, 2013). Richmond Mines interpreted the IP chargeability response to be correlative to graphitic sediments intersected in most holes.

Many surveys have been done in the light of the results of these surveys. In this study, EM and magnetic data-sets are addressed. In the 1980s, a lode gold mineralization was discovered at Deer Cove, Baie Verte Peninsula located north of the Cripple Creek property (Swinden et al., 1991).

In the late 1980s, Esso Minerals' work resulted in a gold discovery in the Weir's Pond area associated with quartz-carbonate alteration within mafic and ultramafic rocks. Grab samples resulted in up to 650 ppb Au, and nine holes were drilled with the best assayed 2.5 g/t Au over 10 cm (Lenters, 1988).

In 2005, grab samples were collected over mineralization zones exposed in 2 outcrops with a length of 20 metres which is located approximately 125m west-northwest of the Cripple Creek showing. The best grab sample assay was 22.9 g/t Au, 6.8% Cu, and 14.4 g/t Ag.

In 2006, 7 holes were drilled to test the hand showings. The best assay from drilling was 2.07 g/t Au over 0.5m, and the best copper result of 0.27% over 0.5m. Pilgrim (2006) suggested that the IP chargeability response correlates to graphitic sediments seen in the drill holes.

Also, between 2009 and 2011, other discoveries were shown with high-grade showings in the area. The details about previous work are given in Nahnybida and Willett (2013).

In the light of these findings, in 2012, an airborne geophysical survey, comprising TEM and magnetic data, was conducted over the whole Cripple Creek area (see Fig. 5.1 and 5.2). In addition to the TEM and magnetic surveys, a ground frequency-domain EM survey was carried out to follow up on all the previous work and responses seen in the airborne TEM data. The results will be given and discussed in the next chapter.

In this study, I focused on the conductor that is located in the core survey area because it is the location with the main mineralization showings, and the conductor response is very clear and discrete in the TEM result. Therefore, I think that this conductor is very probably associated with the mineralization (see Fig. 5.2).



## 5 Prior to Inversion

The data studied in this thesis are the helicopter-borne time-domain EM (VTEM) data-set and the Total Magnetic Intensity (TMI) data-set that were collected together over the entire property in 2012 by Geotech. The survey was designed to cover the entire property at 100m line spacing except for only the core area, which was covered at a 50m line spacing. The TEM and TMI data used in this study were only over the core area that includes the massive sulphide showings (see Fig. 4.3). The survey lines were oriented at 140 degrees azimuth. The survey was completed between May 14<sup>th</sup> and May 21<sup>st</sup>, 2012.

The TEM data were collected over the entire property of 65 km<sup>2</sup>. The total length of survey lines collected was 869.4 km. The helicopter flew at an altitude of 73 m above the ground with an average survey speed of 80 km/h. That means the average EM bird terrain clearance was 42 m, and magnetic sensor clearance was 49 m (see Fig. 2.7).

In the TEM data acquisition, thirty-two time measurement gates were used in the range from 0.096 to 7.036 millisecond (see Table 4.1). The details of the TEM measurement system are presented in Section 2.2.3. For magnetic data acquisition, a Geometrics Cesium vapour magnetometer was used with a sensitivity of 0.001 nT.

The exploration work done in 2012 included a frequency-domain EM (HLEM) survey on the core area and grid soil sampling alongside the airborne geophysical measurements.

Table 5-1 TEM data decay sampling scheme. The times used in the data are given in the "Middle" column.

Channel	Middle	Start	End
Millisecond			
14	0.096	0.090	0.103
15	0.110	0.103	0.118
16	0.126	0.118	0.136
17	0.145	0.136	0.156
18	0.167	0.156	0.179
19	0.192	0.179	0.206
20	0.220	0.206	0.236
21	0.253	0.236	0.271
22	0.290	0.271	0.312
23	0.333	0.312	0.358
24	0.383	0.358	0.411
25	0.440	0.411	0.472
26	0.505	0.472	0.543
27	0.580	0.543	0.623
28	0.667	0.623	0.716
29	0.766	0.716	0.823
30	0.880	0.823	0.945
31	1.010	0.945	1.086
32	1.161	1.086	1.247
33	1.333	1.247	1.432
34	1.531	1.432	1.646
35	1.760	1.646	1.891
36	2.021	1.891	2.172
37	2.323	2.172	2.495
38	2.667	2.495	2.865
39	3.063	2.865	3.292
40	3.521	3.292	3.781
41	4.042	3.781	4.341
42	4.641	4.341	4.987
43	5.333	4.987	5.729
44	6.125	5.729	6.581
45	7.036	6.581	7.560

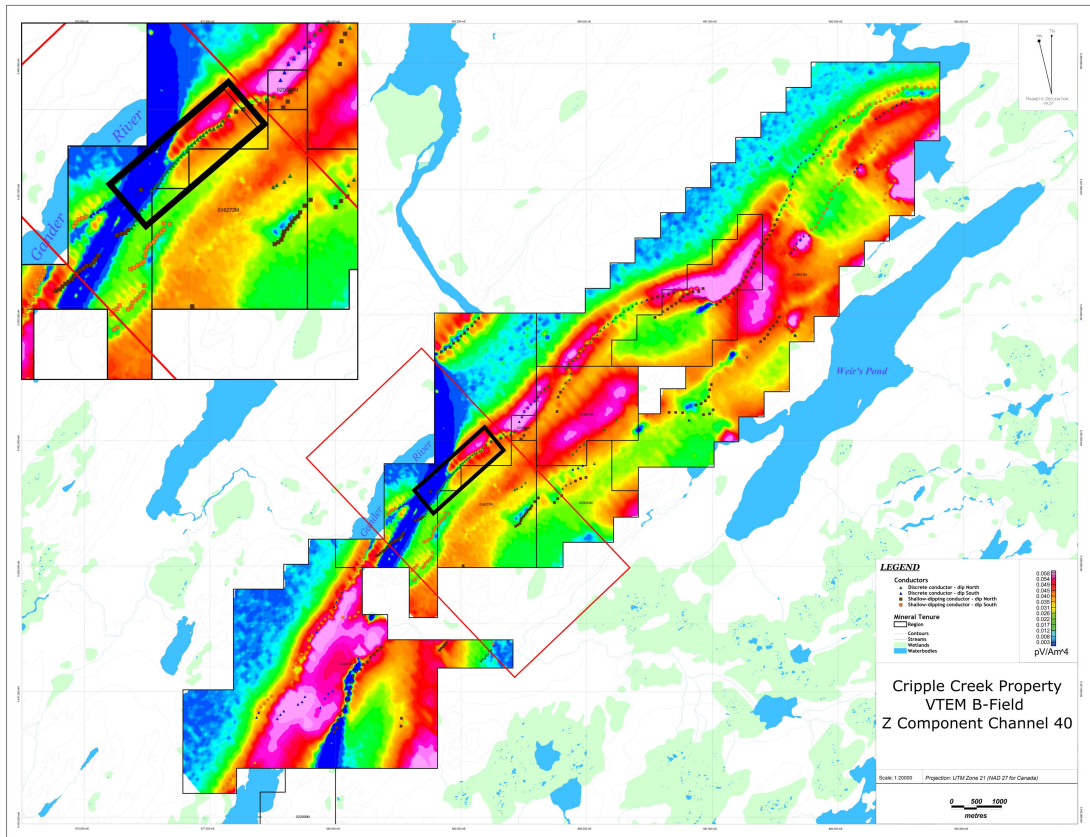


Figure 5.1 The Z component of the VTEM data for the whole of the Cripple Creek survey (Channel 40, see Table 4.1). Conductive trends, corresponding to the larger values on this map, are seen all over the Cripple Creek Property. The red rectangle shows the core area, and the black rectangle within the red one shows the area immediately surrounding the conductor of interest in this study. (Adapted from the Geotech Ltd. Report, 2012.)

In the Geotech Ltd. Report (2012), the airborne TEM and magnetic results were presented as images at a scale of 1:20,000 (see Fig. 5.1 and 5.2). As seen in Figure 5.1, which shows the z-component TEM response at channel 40, many EM anomalies are present across the entire property. Most of the conductors are dipping, plate-like, as given by details in legend.

Looking carefully at Fig. 5.1, all the red areas, (i.e., the areas of high B-field response at this channel), are likely due to overburden or maybe rock type in the area. There is no detailed background about geology for the area for now. So, it is highly likely due to overburden. Also, looking at Fig. 5.3 and 5.4, the high responses at all channels in the middle part of this graph are continuous high values for multiple kilometres along the line, which corresponds to red areas in Fig. 5.1. The responses in Fig 5.3 and 5.4 are typically a layered Earth response that is not so changing along the survey line. In contrast, the feature in the left of the profile, i.e., the two peaks with quite a deep central trough can only be coming from a localized 3D feature in the subsurface.

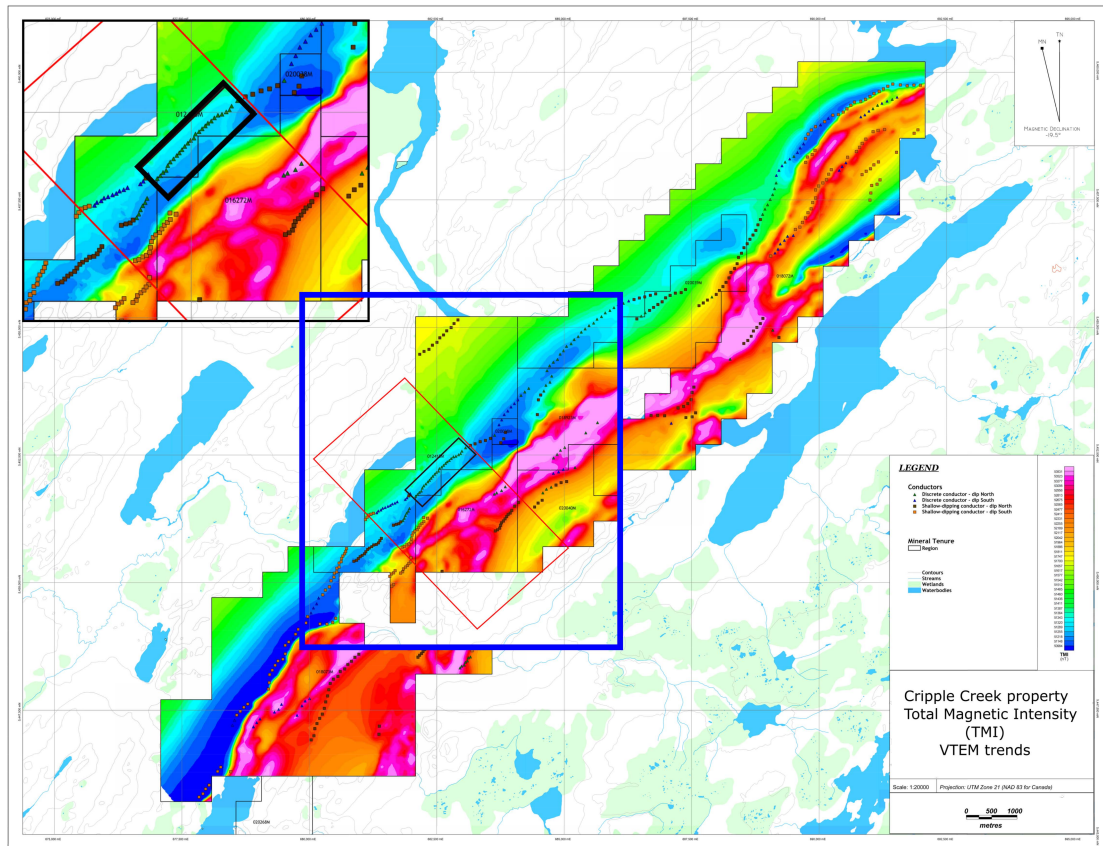


Figure 5.2 The Total Magnetic Intensity (TMI) for whole Cripple Creek Property. The red rectangle shows the core area (and the magnetic data used), and the black rectangle in the red one shows the conductor of interest. The blue one shows the area for the inversion (Adapted from the Geotech Ltd. Report, 2012.)

As discussed in Section 3, with the fast interpretation by using shaped plate models, the conductor of interest shown in Fig. 5.1 was evaluated along with the TEM and HLEM responses together. The location and the geometry of the conductor were determined from the overlap of the TEM and HLEM responses.

### TEM L2290 and HLEM 11700

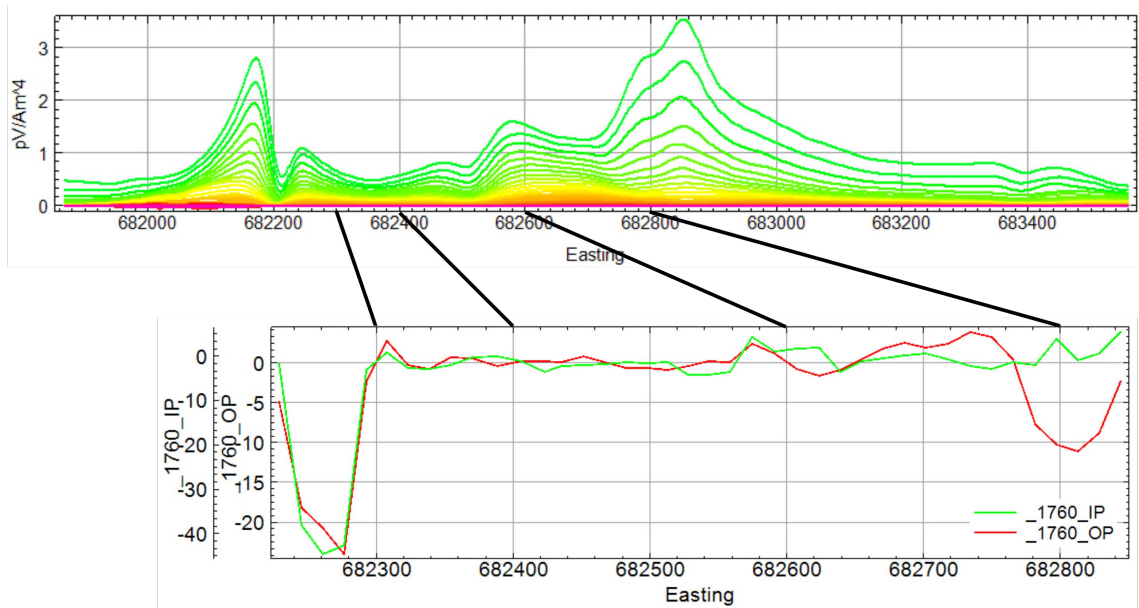


Figure 5.3 Comparison of the TEM and HLEM responses along one pair of co-incident lines. The z-component of the TEM response for line L2290 is shown at the top. The HLEM response for line 11700 is shown at the bottom. The coloured lines on the top plot are the time gates in Table 5.1. The red and green lines on the lower plot represent the out-of-phase and in-phase components at 1760 Hz.

The TEM and HLEM measurements along two pairs of overlapping survey lines are given in Fig. 5.3 and 5.4. As seen in Fig. 5.3 in the TEM response, at an x-coordinate of around 682200m, there is a two-peak response, which is an indicator of a steeply inclined thin plate-like conductor dipping to the left-hand end of this plot (which is to the north-west; Fig. 3.1). Also, the valley-like response at the left-hand end of the HLEM plot is indicative of the same kind of conductor. There are little offsets in the locations of the conductor responses in the TEM and HLEM profiles in Fig. 5.3 and Fig 5.4. In Fig. 5.3, according to the TEM response, the conductor is centred on the x-coordinate of 682200m, whereas in the HLEM

response, the conductor is centred on the coordinate of 682280m. That is, there is an 80 m difference between the locations of the two responses. This might be because of the GPS sensitivity during airborne data acquisition. Since ground-based systems are more sensitive and reliable for determining the locations of the anomalies, it is assumed that the conductor of interest is located on the x-coordinate of 682280m.

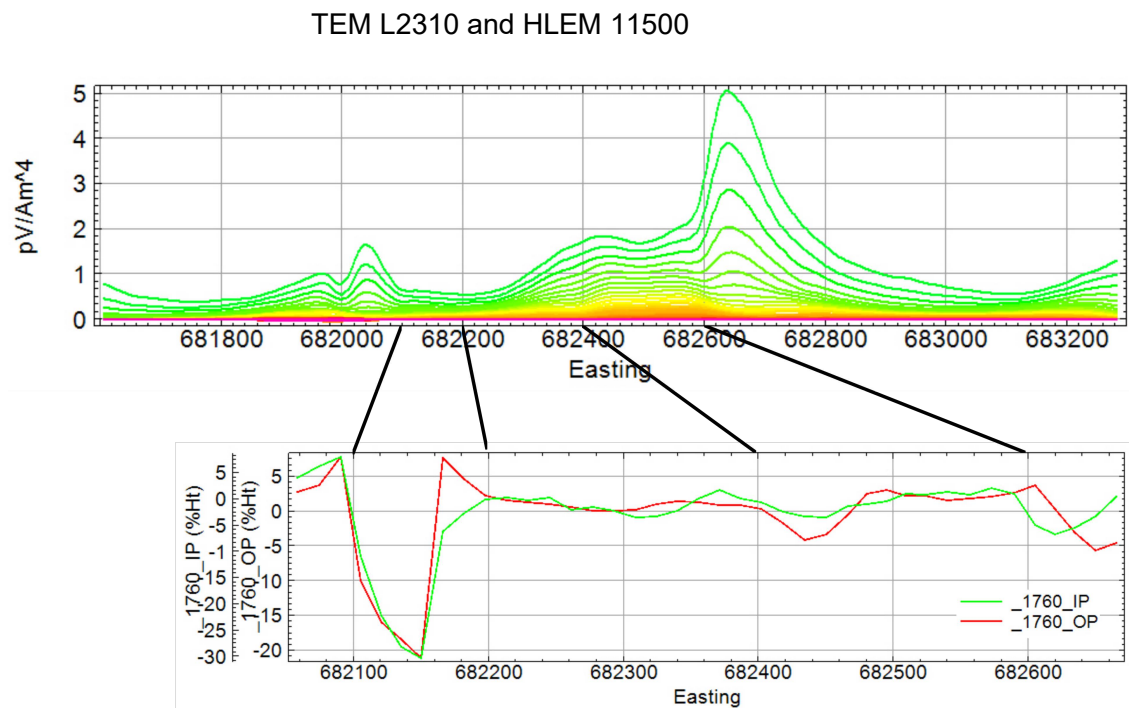


Figure 5.4 Comparison of the TEM and HLEM responses along one pair of co-incident lines. The z-component of the TEM response for line L2310 is shown at the top. The HLEM response for line 11500 is shown at the bottom. The coloured lines on the top plot are the time gates in the Table 5.1. The red and green lines on the lower plot represent the out-of-phase and in-phase components at 1760 Hz.



As seen in the TEM response in Fig. 5.4, there is a two-peak response at around an x-coordinate of 682120m, which is an indicator of an inclined thin plate-like conductor steeply dipping to the right-hand end of the plot (which is to the south-east in real). Although it is clearer on L2290 (see Fig. 5.3), it is seen on L2310 as well. It should be noticed that the higher peak on L2310 is located on the right-hand side of the response. This means the conductor dips to the right-hand side in the subsurface, east in reality, as opposed to as with L2290 (see Fig. 3.1).



## 6 Inversion and Modelling

### 6.1 1D Inversion of The Cripple Creek VTEM data

1D TEM inversion is done with program EM1DTM, as discussed in Section 3.3. In the TEM data inversion, measured voltage values from the receiver are used. These voltage values include the differentiation of the secondary  $B$ -field called  $dB/dt$ , and they have been recorded as picovolt ( $pV$ ). The model has 50 layers that logarithmically increase the thicknesses with depth up to 651 m. As the starting model, the conductivities of the layers are set to  $1.0E-2 S/m$ . As mentioned in Section 3.4.1, there are four different algorithms available in EM1DTM for determining the trade-off parameter. All of them were tried, with the user-supplied cooling schedule found to give the best results. In order to determine the inversion parameters, a trial-and-error process was done, and a starting  $\beta$ -value of 1000 was used. The trade-off parameter is then halved at each iteration until the value of 10 is reached, beyond which the value of 10 is used. A maximum of 30 iterations was found to be sufficient. The inversion stops after the maximum number of iterations or if there is no remarkable difference between the objective function and the model parameters from the previous iteration.

The inversion was done flight-line by flight-line on the entire core area (see Fig. 5.1). The program EM1DTM inverts soundings for only a 1D medium. The resulting conductivities of the layers were plotted as pseudo-2D cross-sections

using MATLAB code that I wrote. Since every survey line has a different number of soundings, the location of the conductor in the 2D cross-sections is not always beneath the same sounding number. The inversion results for lines L2310, L2290, L2270, L2250, L2230, and L2210 are shown in Fig. 6.1. (Larger values of the panels in Fig. 6.1 are given in Appendix A.)

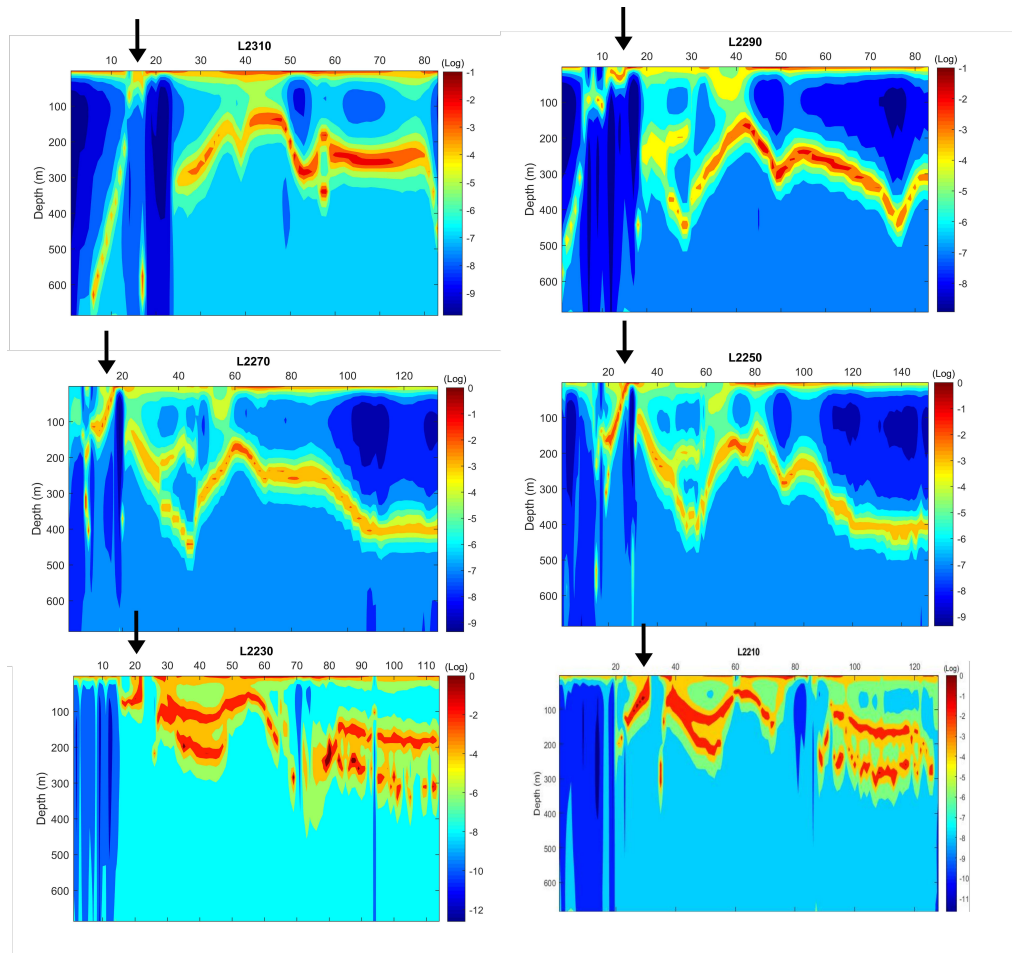


Figure 6.1 2D cross-sections made from the TEM 1D inversion results over the main area of interest (see Fig. 5.5 for the locations of the flight lines). The arrows show the location of the conductor. The colour bar shows the conductivity in log scale ( $S/m$ ). Larger values of these sections are given in Appendix A.

The conductor of interest is visible in Fig. 6.1. Also, a relatively conductive overburden is obvious, as well. However, it is highly likely that the horizontal conductive trend between 200 and 500 metres depth for all lines is an artifact. This is the main disadvantage of EM methods. They are getting unreliable with depth due to the decay of the EM field and the data at later times getting noisy.

The conductor of interest, which is visible on the responses in Fig. 5.2 that has a direction to the north-west, is consistent with the inversion model of L2290 in Fig. 6.1. The conductor of interest, which is visible on the responses in Fig. 5.3 that has a direction to the south-east, is relatively consistent with the inversion model of L2310 in Fig. 6.1. In the inversion model of L2310, the conductor is a little bit subtle compare to L2290. Even so, both of them are consistent with the responses in Fig. 5.2 and 5.3. As a result, the dips of the conductor in two different responses and the inversion models are consistent with each other.

Prior to making a decision on whether or not an inversion result is reasonable, one should look at the data misfit between observed data and predicted data for the constructed inversion models. Firstly, to see the data misfit in detail, the misfit of four soundings, which are located just over the conductor of interest, are shown in Fig. 6.2. The peaks and troughs on the observed data at middle and late times result from the sign changes in the observations, which result from the direction of the secondary magnetic field changing in the receiver. The measured values of the z-component at the centre of the transmitter loop will always be

positive for a horizontally layered Earth (see Fig. 3.1 and 3.2.) So, getting negative values for a central-loop transmitter-receiver configuration is essentially just noise.

It is clear that the fit is good enough in the earlier times, which means the inversion result is more reliable in shallow depths. The data at middle and late times are noisy, in fact, full of noise with no real signal coming from the subsurface.

The fit of all the soundings over the conductor is shown in Fig. 6.3. It is essential to look at the data misfit of the other soundings together to get a conclusion on whether the inversion is good enough or not. As seen in Fig. 6.3, early times (the data with the larger values for each sounding in Fig. 6.3) have a good match, which means that the shallow parts of the constructed models are likely reasonable (in which the conductor of interest is located), whereas the middle and deeper parts of the constructed models are not likely to be correct. This pattern can be seen in all other soundings as well.

The first measurement time in the receiver is approximately  $7.3\text{ ms}$ . On the plots of the sounding curves in Fig. 6.2, the data look good only up until approximately  $8.0\text{ ms}$ . This is a time of approximately  $0.7\text{ ms}$  after the transmitter was turned off. This time gives us an indication of depth above which the inversion result is reliable after a simple calculation using the skin depth formula for the time domain (see

Eq. 2.5d). I have considered a time of 0.5 *ms* as corresponding to data that are still clearly above the noise. An average, representative conductivity is used in the skin depth calculation. If there is a thicker layer of higher conductivity, the skin depth gets less for the given time, which means that we would be getting artefacts at shallower depths below areas of thicker overburden. When 0,5 *ms* is used in the skin depth formula with 0.01 *S/m* as a representative conductivity, the reliable depth of the inversion is 282.09 *m*. Looking at Fig. 6.1, the artefacts are mostly happening at depths approximately below 200 – 250 *m*.

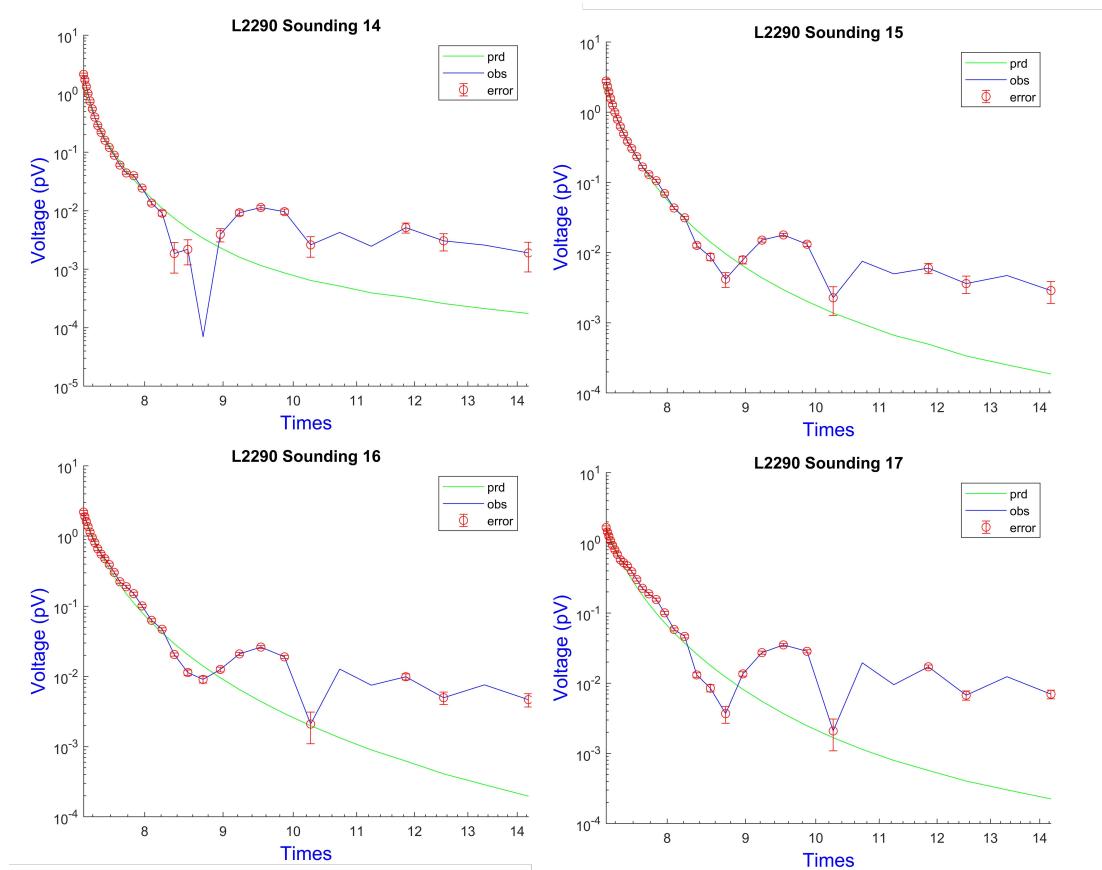


Figure 6.2 The fit between observed and predicted data. The green line and the blue

line represent the predicted and the observed data, respectively. X-axes shows time gates. The red signs show the estimations of the error in the observations. The peaks and troughs on the observed data later than approximately 9ms result from the sign changes in the observations. The absolute values of the observations are plotted.

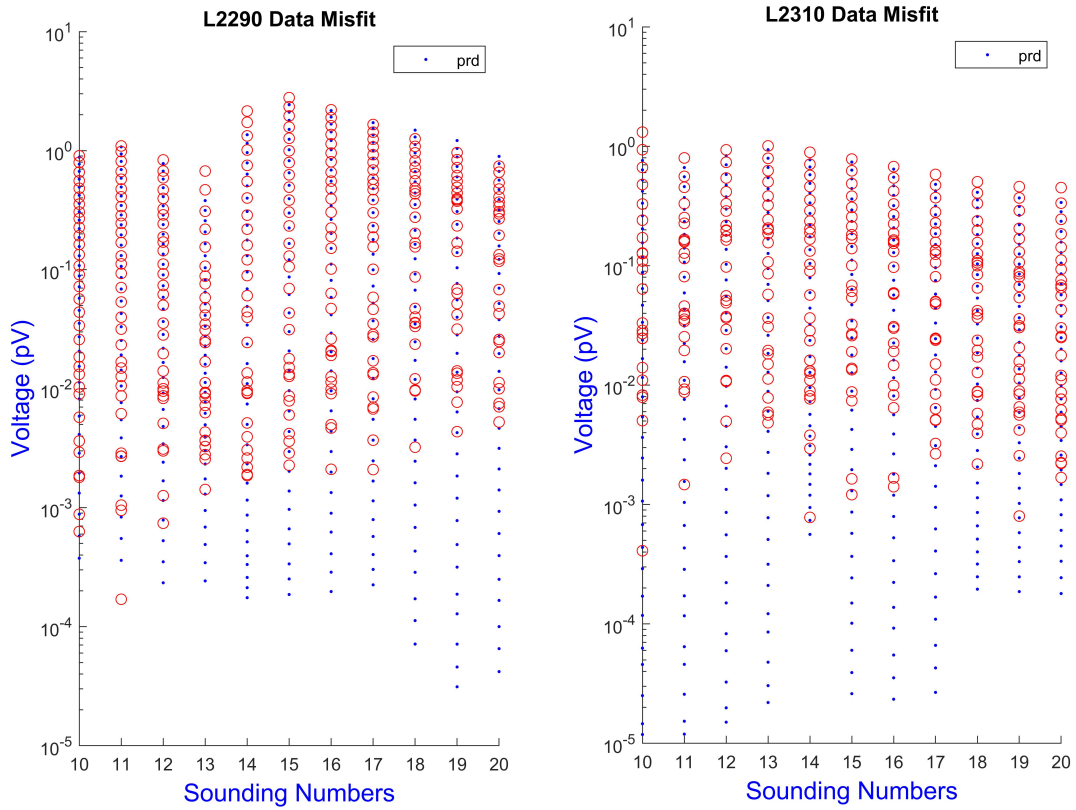


Figure 6.3 The observed and predicted data of the L2290 and the L2310 survey lines. Ten soundings over the location of the conductor are used. The blue points and the red circles represent the predicted and the observed data, respectively.



## 6.2 Maxwell Modelling

For a better understanding of the depth and geometry of the plate-like conductor, modelling work is done with the program Maxwell. Models were made and responses computed to try to get the same TEM and HLEM responses as the observed data-sets (that is, the data presented in Fig. 5.3 and 5.4). The best models that were obtained for lines L2290 and 11700 are shown in Fig. 6.4. The parameters of the models are given in Table 6.1.

The models for the TEM and HLEM data are not consistent with each other. The locations of the responses are not exactly the same, as mentioned above. There is approximately 80 *m* difference between them. There might be a mis-location in one of the data-sets. They might be different conductors. Possibly, the airborne TEM measurement managed to observe the deeper, large plate (according to the Maxwell modelling) under L229 but missed the HLEM anomaly of the shallower, small plate under line 11700. The HLEM measurements are more sensitive to the shallow conductors. Plus, the conductor of line 11700 is closer to the Earth's surface. Also, it is thinner, 1 m thickness, and has a 30° dip angle, which means it is nearly horizontal. Otherwise, they might be the same conductor, and it may have complex geology.

Table 6.1 The specifications of the Maxwell models for the TEM survey line L2290 and the HLEM survey line 11500.

<b>L2290 TEM</b>						
Easting	Nothing	Depth	Dimension	Dip	Rotation	Conductivity
682 218	5 451 780	-10 m	90x150 <i>m</i>	70°	0°	25 <i>S/m</i>
<b>11700 HLEM</b>						
Easting	Nothing	Depth	Dimension	Dip	Rotation	Conductivity
682 307	5 451 697	-7 m	80x80 <i>m</i>	30°	40°	25 <i>S/m</i>

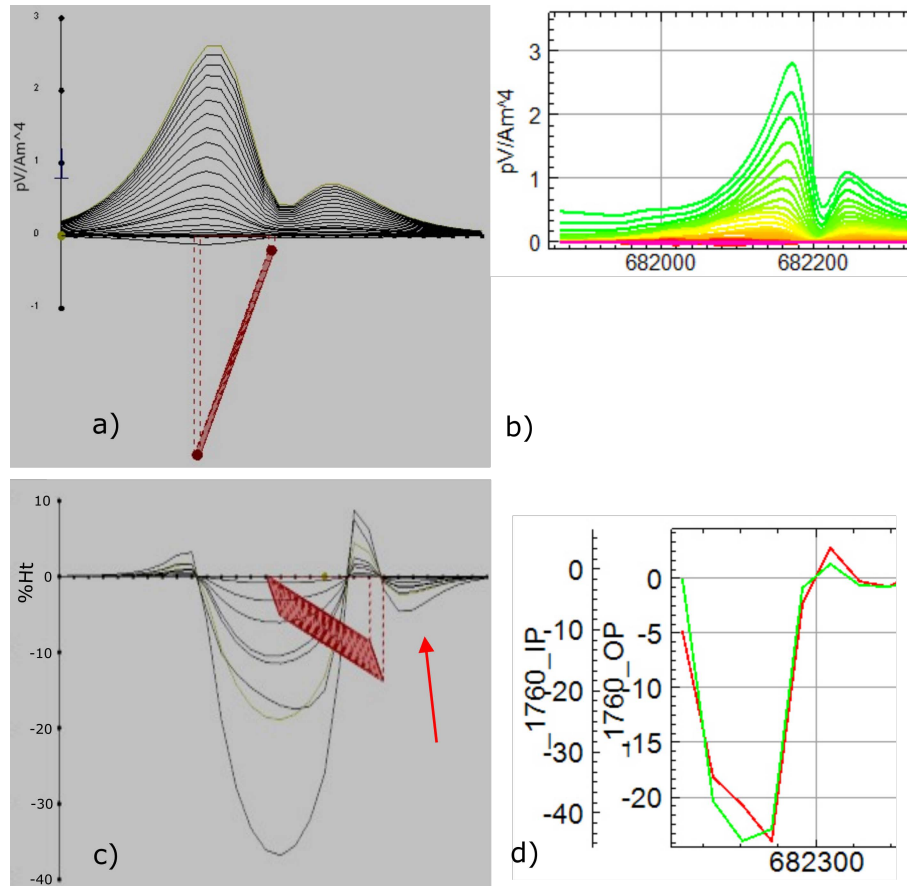


Figure 6.4 a) The airborne TEM synthetic response over a Maxwell model. b) The airborne TEM observed response for line L2290. c) The ground HLEM synthetic response over another Maxwell model. d) The ground HLEM observed response for survey line 11700. The specifications of the models are given in Table 6.1. The red arrow shows the negative side-lobe values.

The conductors seen in the TEM and HLEM data-sets are possibly different. The HLEM response over the same Maxwell model as for the TEM data are presented in Fig. 6.5. The model is entirely the same as for the TEM survey line L2290. That is, in Fig. 6.5, the TEM response is identical with the data shown in Fig. 6.4 and matches the shape of the two-peak anomaly in the airborne TEM

data, and the HLEM response over this model is shown as well. This means that if the TEM data and the HLEM data were seeing the same conductor, the HLEM response would be like that in Fig. 6.5. In addition, the negative side-lobes in Fig. 6.4, shown by the red arrow, prove that the conductor is stretching to the right.

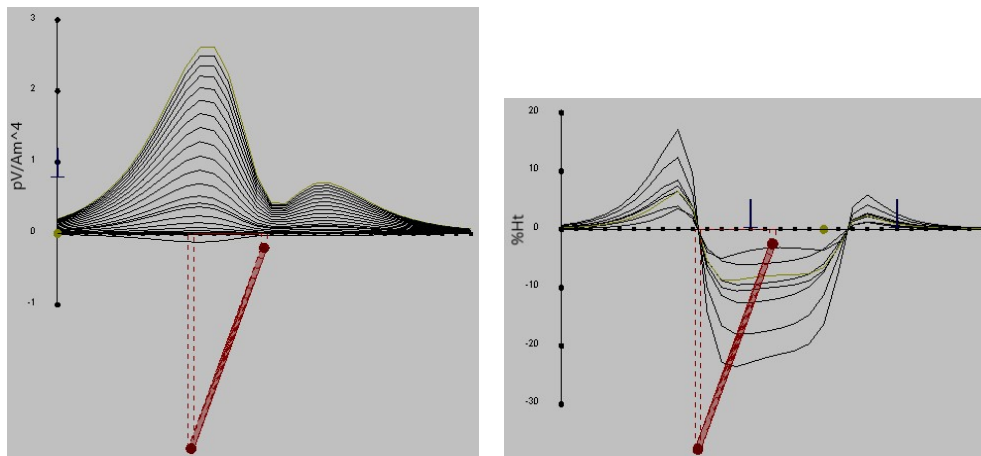


Figure 6.5 TEM (left; same as in Fig. 6.4) and HLEM responses (right) over the same model as for line L2290 (airborne TEM data).

Modelling was also done for the TEM survey line L2310. The model for the HLEM survey line 11500 is made. The specifications of the model are given in Table 6.2.

Table 6.2 The specifications of the Maxwell models for the TEM survey line L2310 and the HLEM survey line 11700.

<b>L2310 TEM</b>						
Easting	Nothing	Depth	Dimension	Dip	Rotation	Conductivity
682 000	5 451 734	-10 m	90x120 <i>m</i>	80°	0°	9 <i>S/m</i>
<b>11500 HLEM</b>						
Easting	Nothing	Depth	Dimension	Dip	Rotation	Conductivity
682 090	5 451 653	-10 m	90x120 <i>m</i>	80°	0°	9 <i>S/m</i>

It is clear how the models for the two different data-sets presented in Fig. 5.4 are consistent. However, again there is 80 *m* difference between them. They are probably the same conductor, and there may be a GPS issue during the measurements. However, they might not be the same conductor as well. We will have a better interpretation and conclusion after the inversion process.

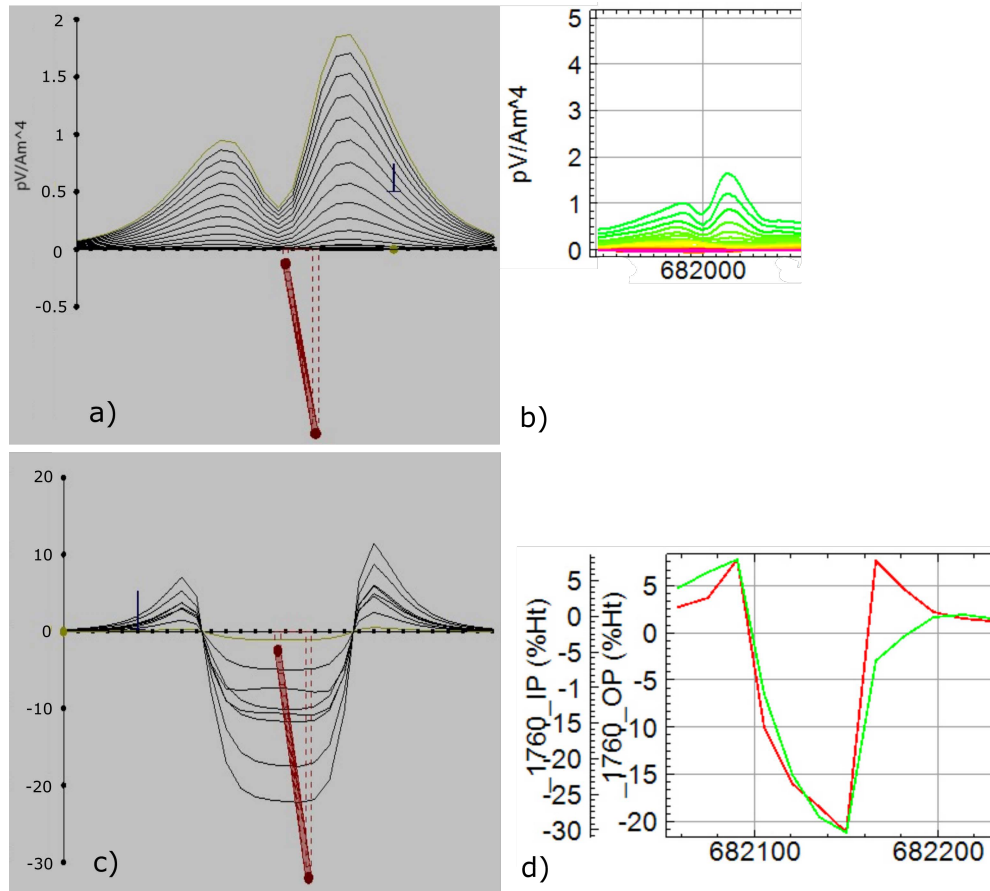


Figure 6.6 a) The airborne TEM synthetic response over a Maxwell model. b) The airborne TEM observed response for line L2310. c) The ground HLEM synthetic response over another Maxwell model. d) The ground HLEM observed response for survey line 11500. The specifications of the models are given in Table 6.2.

### **6.3 TEM 3D Modelling**

To concatenate all of the 2D cross-sections over the entire core area, for getting a nice 3D picture for a better interpretation, the program EM1D3D was used. It is a utility program that comes with EM1DTM that interpolates the 1D inversion results to a 3D rectilinear mesh. The program Paraview is then used for visualization of the mesh-based result (see Fig. 6.1).

The conductor's shape and depth are more clearly seen in Fig. 6.1 than 2D cross-sections because 3D TEM models provide us scaled pictures of the whole area. Hence, all of the details have become noticeable with 3D modelling.

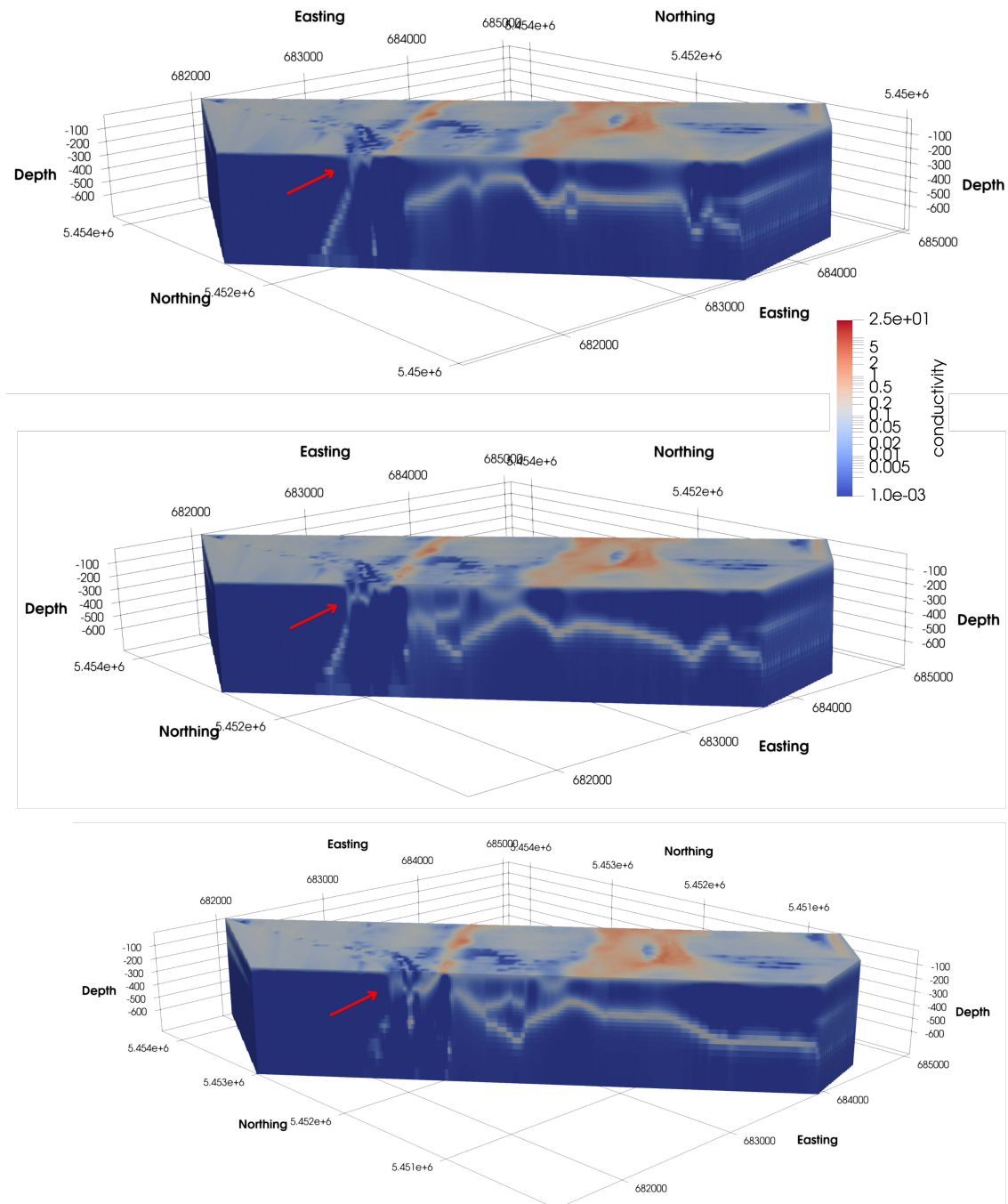


Figure 6.7 3D images of the 1D TEM inversion result for survey lines L2310, L2290, and L2270. The red arrows show the conductor of interest.



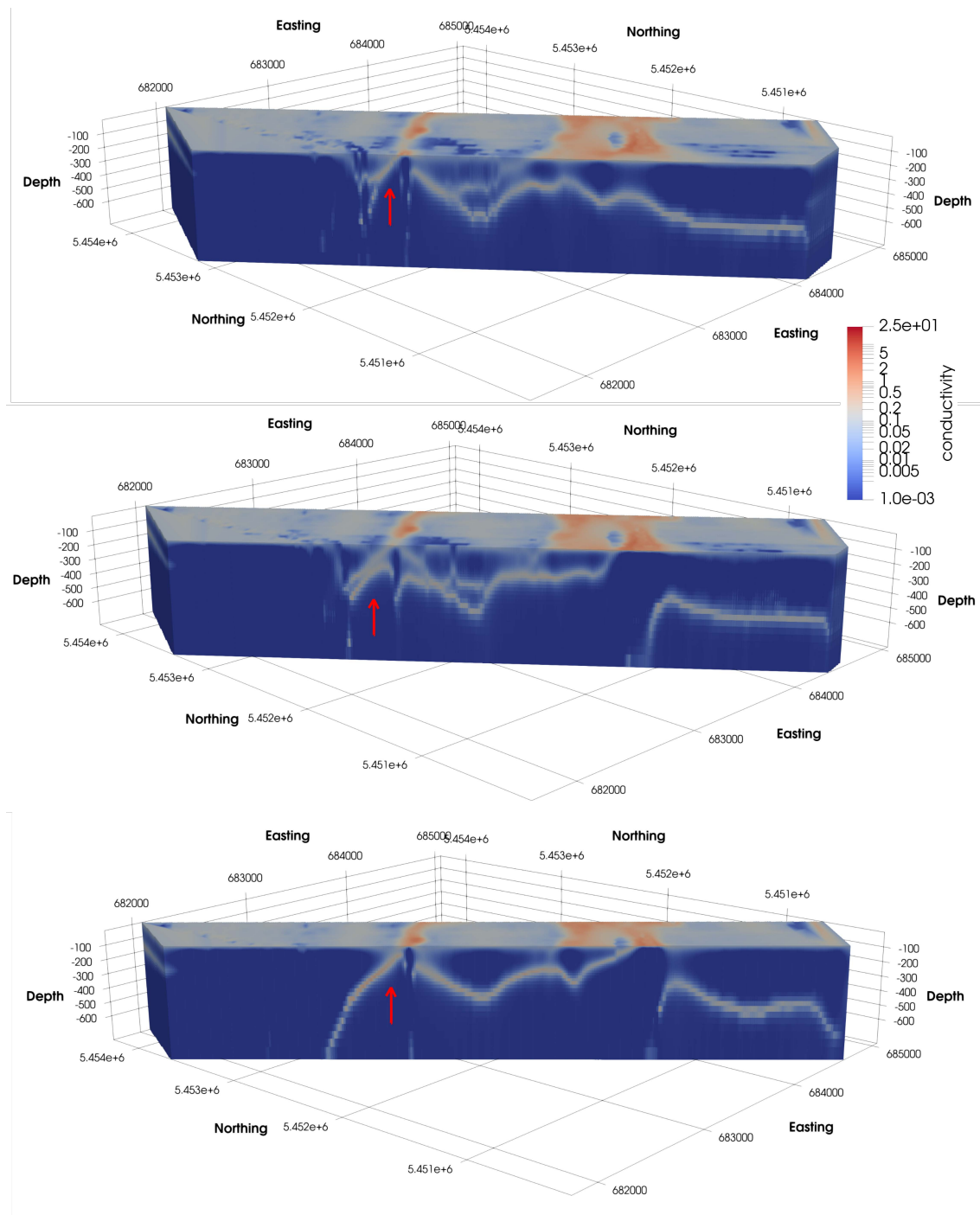


Figure 6.8 3D images of the 1D TEM inversion result for survey lines L2250, L2230, and L2210. The red arrows show the conductor of interest.

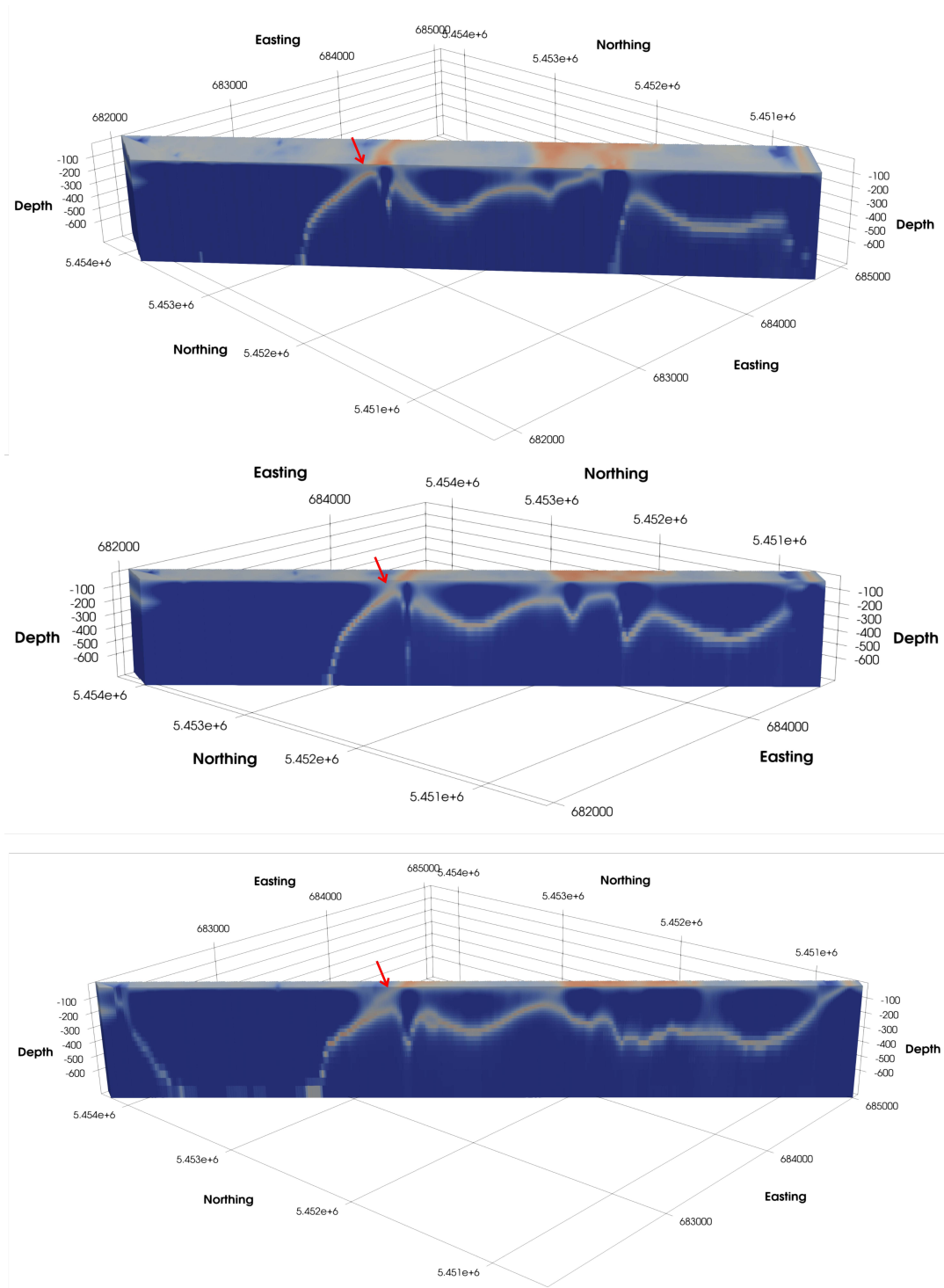


Figure 6.9 3D images of the 1D TEM inversion result for survey lines L2190, L2170, and L2150. The red arrows shows the conductor of interest.

## 6.4 3D Inversion of The Magnetic Data

3D magnetic inversion is done here with the code VIDl, discussed in Section 3.4.2. The region of interest (see Fig. 5.2) is discretized into rectilinear meshes. The grid used consists of cells of 65m in each lateral dimension beneath the observation points with an increased dimension of 200m in padding cells. In the z-direction, the cells of 50m and 100m in depth extent are used. The total number of grid cells is 223,123.

A constant value was removed from the TMI data to give the anomaly data that were inverted. The value removed was 52235 nT which corresponds to the Earth's field in the centre of the survey area at the time of the survey (inclination 69° and declination -20°). The number of data used is 2120 (see Fig. 6.10). The survey lines from L2150 to L2430 are used for the magnetic inversion with 200m line spacing. The lengths of the survey lines vary from 2km to 3.5km with the station spacing of 30m. The survey lines used for the TEM and magnetic inversions are the same, with different lines and station spacings. However, the mesh for the magnetic inversion is larger than for the TEM inversion (see Fig. 5.2). The airborne measurement was carried out with the station spacing of 3m. I wrote a MATLAB code to select one observation point from every ten locations so that the station spacing would be 30m.

The initial lambda trade-off parameter that was used was  $1.0\text{E-}1$ . At the end of the inversion, the trade-off parameter reached the value of  $3.0779\text{E+}03$ . The sensitivity weighting is used with the norm of 2.0 and the beta of 1.0, as discussed in Section 3.4.2. This inversion took 48 iterations to reach the target normalized misfit of 1.0. The more important parameter showing that the inversion is acceptable is the normalized data misfit. It can be seen which parts of the data are fit better than others. If the data residuals look like random noise (like this inversion, see Fig. 6.11), that means the inversion is acceptable.

A slice from the 3D susceptibility model produced by the magnetic inversion and a slice from the 3D picture of the TEM inversion results are presented in Fig. 6.13. The indication of the conductor of interest is seen clearly on the TEM constructed model (bottom in Fig. 6.13), whereas it is a little bit subtle on the constructed model of the magnetic inversion (top in Fig. 6.13). Both represent exactly the same location in the survey area, which is beneath the TEM survey line L2220. The magnetic result is utterly consistent with the TEM inversion result and the Maxwell models as well. The conductor is only a little bit longer in the magnetic result. However, the top point of the conductor is very consistent with the Maxwell models, which is -10m.

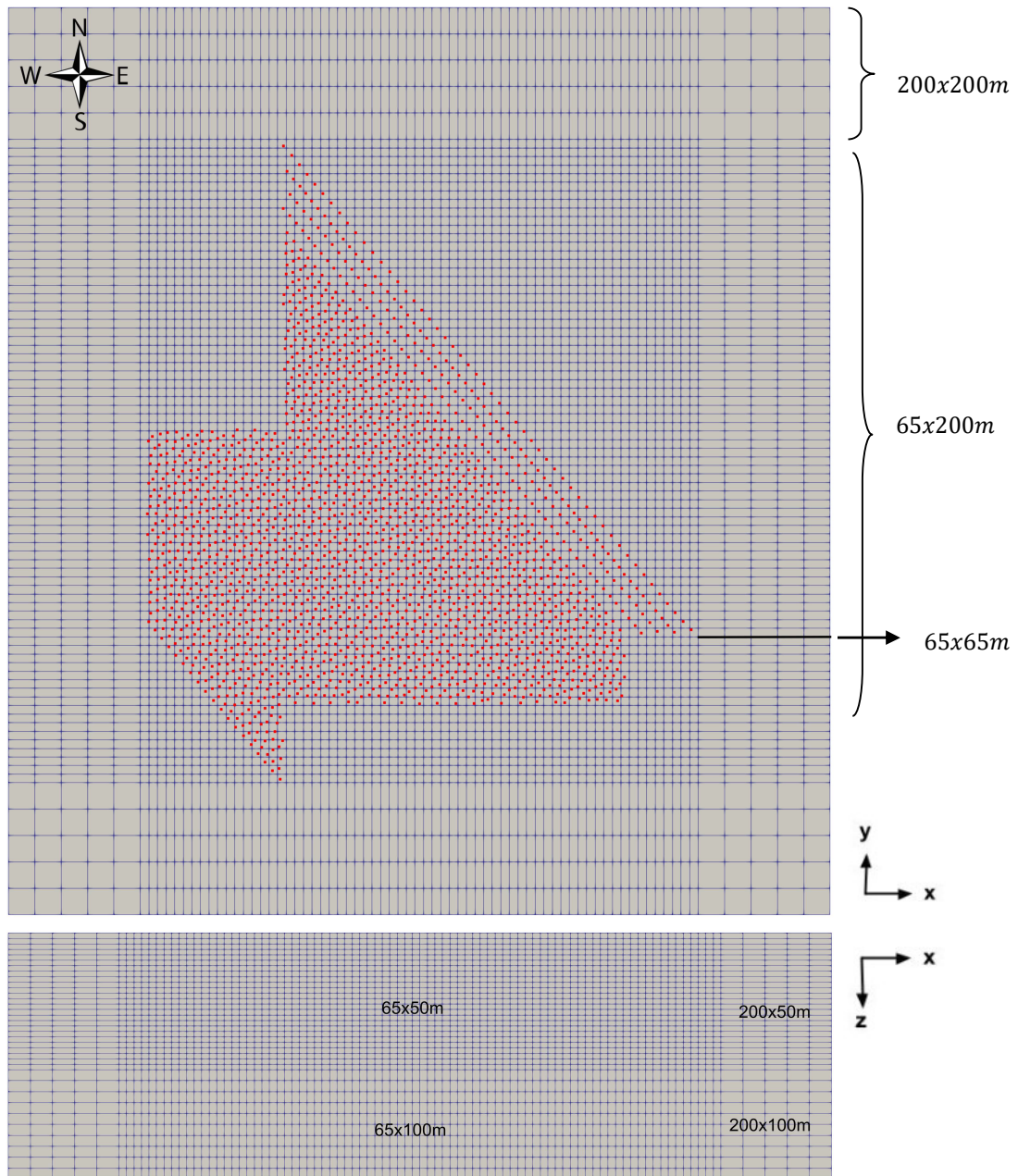


Figure 6.10 The mesh used for the 3D magnetic inversion. The top picture is the x-y section, along with the observation locations (red points). The coordinates of the corners of the top picture from top-two to bottom-two are 679900.6E - 5454749.5N, 686125.6E - 5454749.5N, and

679900.6E - 5448524.5N, 686775.6E - 5448524.5N. z-coordinates are 59.9 for all four points because the mesh has a flat surface. The bottom picture is the x-z cross-section view.

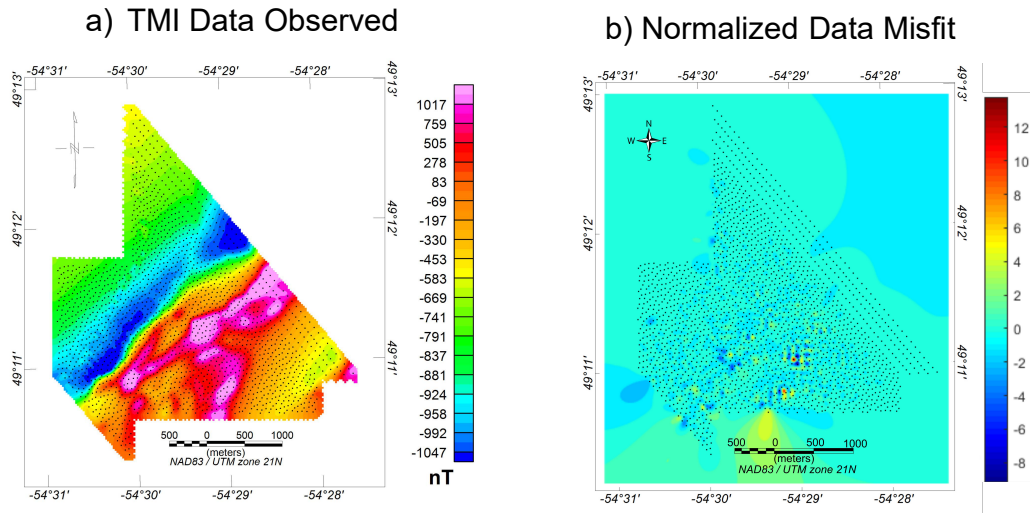


Figure 6.11 a) The observed total-field magnetic anomaly. b) The normalized data misfit of the magnetic inversion under the observation points.

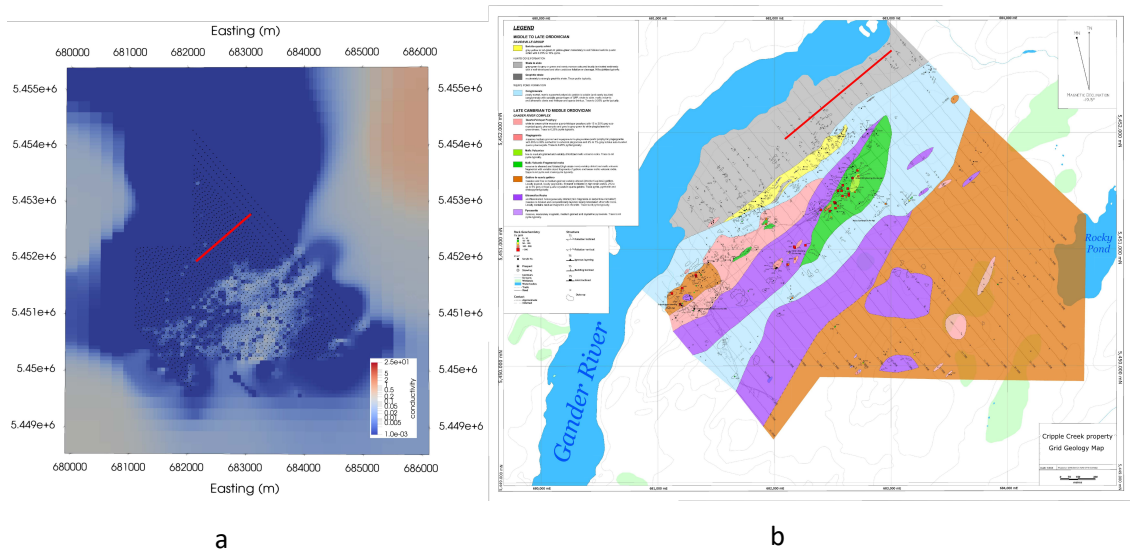


Figure 6.12 a) Plan view of the 3D magnetic inversion model. b) Geology map and the mineralization showing the core area. The red lines show the location of the conductor of interest that is dipping north-west.

The conductor of interest is located over the non-magnetic formation, as seen in Fig. 6.12a. The non-magnetic formation, which is grey on the geology map, is shale to slate. This shale is grey or green and rarely maroon coloured locally laminated sediment with a well-developed and often undulose foliation or cleavage known nil sulphides. However, the conductor is also located north-west of high susceptible formations. This high-susceptible unit consists of mafic volcanics, ultramafic rocks, gabbro, and quartz-feldspar porphyry. Mafic volcanics include high Cu ppm (see Fig. 6.12b). The 3D magnetic inversion revealed the magnetic properties of the rocks around the core area. These non-magnetic and magnetic units continue throughout from south-west to north-east. Possibly, there might be similar conductors along the strike.



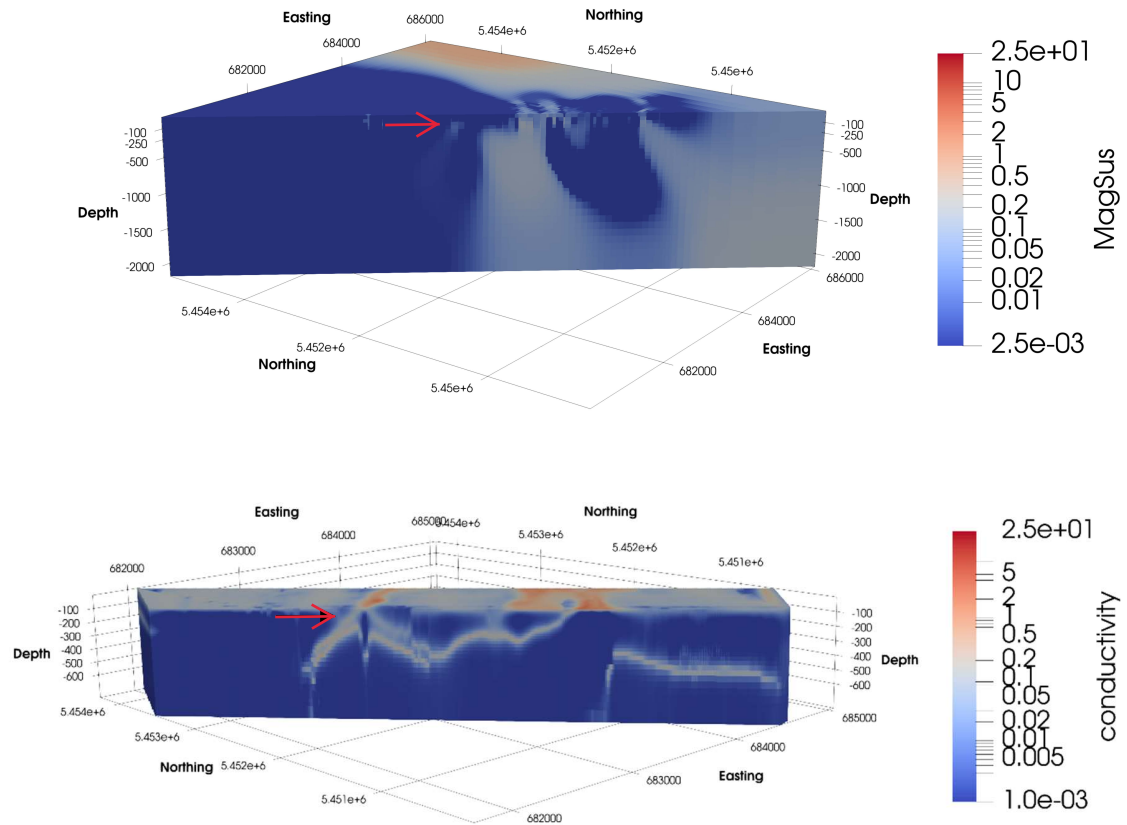


Figure 6.13 A slice through the 3D susceptibility model constructed by magnetic inversion (at the top) and a slice through the 3D conductivity model from the 1D TEM inversion results (at the bottom). The slices are along survey line L2220. The red arrows show the conductor of interest. The units of the easting, northing, and depth are metres. The unit of the conductivity is S/m.



## 7 Summary and Conclusion

The Cripple Creek property is located in eastern Newfoundland. It is an ancient Volcanogenic Massive Sulphide area (VMS) covering two tectonostratigraphic zones, the Dunnage Zone and the Gander Zone. The Gander River Complex is a geological formation between these two zones, which is an ophiolite comprising ultramafic to felsic plutonic rocks and mafic volcanic rocks.

The VMS deposits include Au, Cu, Zn, Ag, and Sb as main minerals. They are also significant resources for Co, Sn, Se, Mn, Cd, In, Bi, Te, Ga, and Ge. The remarkable Au value in the area of interest up to 19 g/t Au is associated with up to 15.5% Cu and Zn.

Exploration work in the area dates back to the 1930s for a chromite deposit. Since then, a couple of drilling works have been conducted, and many grab samples have been collected. In light of the previous works, a comprehensive geophysical study was carried out in 2012. An airborne time-domain EM along with magnetic measurement and a ground-based horizontal loop frequency-domain EM, also known as Max-Min, was conducted.

The airborne TEM and magnetic survey includes 318 survey lines over the area of 65 km<sup>2</sup>. The 57 survey lines were addressed in this study on which were located the main mineralization zone known as the core area. The frequency-domain HLEM survey conducted in the core area as well includes 6 survey lines.

Firstly, the 1D inversion was carried out for airborne TEM measurements using program EM1DTM. 1D conductivity models were produced at each measurement location. Then, these 1D models were concatenated to produce a 2D cross-section of the subsurface along the survey lines using MATLAB codes. The plate-like conductor could be discerned in the 2D images of the TEM inversion results. The data misfit was calculated to evaluate the results, and it was seen that the inversion results were reliable for shallow depths.

To figure out the details of the shape and geometry of the conductor of interest in the TEM inversion results, modelling was conducted using Maxwell, which is a modelling program generating plate-like models for EM methods. For the survey line L2290 of the TEM and 11500 of the HLEM measurements, which have 80 *m* distance, the Maxwell models were made, and it was seen that two models were not consistent. Another modelling was made for the survey line L2310 of the TEM and 11700 of the HLEM measurements. Two models were quite consistent. However, there is 80 *m* distance between them, too. They might be the same conductor, and there might be a GPS issue, but also they might be separate conductors as well. As a result of two modelling, they are probably separate two conductors, or they are united, but it is a complex structure consisting of multiple plate-like structures.

For a better interpretation, 3D pictures of the TEM inversion results were produced using a subprogram EM1D3D. The structure of the conductor was seen

more clearly in the 3D medium. They have scaled pictures in a 3D medium instead of unscaled 2D cross-sections.

Considering the inversion results and the Maxwell modelling, the conductive structure presumably consists of multiple plate-like conductors. According to the Maxwell models, it is approximately 190 *m* long with the 80° dip angle beneath the TEM survey lines, but it is more shallow in the HLEM responses. The Maxwell modelling has given the idea that it might be a long conductor up to 200 *m*. However, with the inversion process, it is clear that it has a complex structure in a shallow depth, but the inversion might not say more since it is reliable only for shallow. As a result, the conductor of interest might be complicated in shallow, and it might be more plate-like or straight with depth.

As for the magnetic inversion model, the conductor of interest shows a magnetic property beneath the TEM survey line L2220. Also, magnetic inversion has revealed the magnetic susceptibility distribution around the conductor. This is valuable information to interpret the area geologically.

## REFERENCES

Africa J.R. (2013). 1D Inversion of MT and TEM data with application of soundings from Krýsuvík, Sw-Iceland and a review of MT/TEM data from Bacman Geothermal Project, Central Philippines.

Attenuation and Skin Depth, (n.d.). em.geosci.xyz. Retrieved from [https://em.geosci.xyz/content/maxwell1\\_fundamentals/harmonic\\_planewaves\\_homogeneous/skindepth.html](https://em.geosci.xyz/content/maxwell1_fundamentals/harmonic_planewaves_homogeneous/skindepth.html)

Basic Principles of Magnetism, 2017. gpg.geosci.xyz. Retrieved from [https://gpg.geosci.xyz/content/magnetism/magnetism\\_basic\\_principles.html#equation-mkappah](https://gpg.geosci.xyz/content/magnetism/magnetism_basic_principles.html#equation-mkappah).

Blakely, Richard J. (1996). Potential Theory in Gravity and Magnetic Applications, Cambridge: Cambridge University Press.

Christiansen A.V., Auken E. and Sørensen K. (2006). The Transient Electromagnetic Method. Groundwater geophysics, a tool for hydrogeology.

Clark, D. A., and Emerson D. W. (1991). "Notes on rock magnetization characteristics in applied geophysics studies," Exploration Geophysics, 22, 547-555.

Everett Mark E. (2013). Near-Surface Applied Geophysics, Cambridge University Press, p. 213-214.

Exploration on Licences of 12415M, 16272M, 18072M, 18073M, 20038M, 20039M, 20040M, 18923M and 20268M, Cripple Creek Property, Northeastern Newfoundland for 0840559 B.C. Ltd.

- Farquharson C. G. and Oldenburg D. W. (1993). Inversion of Time-Domain Electromagnetic data for a Horizontally Layered Earth, *Geophysical Journal International*, 114, 433-442.
- Farquharson C. G. et al. (2003). Simultaneous 1D inversion of loop-loop electromagnetic data for magnetic susceptibility and electrical conductivity, *Editor, Society of Exploration Geophysicists*, Vol. 68, No. 6, P. 1857-1869.
- Farquharson, C. G., and Oldenburg D. W. (1996). Approximate sensitivities for the electromagnetic inverse problem, *Geophysical Journal International*, 126, 235–252.
- Farquharson, C. G., and Oldenburg D. W. (1998). Non-linear inversion using general measures of data misfit and model structure, *Geophysical Journal International*, 134, 213–227.
- Farquharson, C. G., and Oldenburg D. W. (2004). A comparison of automatic techniques for estimating the regularization parameter in non-linear inverse problems, *Geophysical Journal International*, 156, 411–425.
- Fountain et al. (2005) A helicopter time-domain EM System applied to mineral exploration: system and data.
- Fullagar P.K. (1989). Generation of conductivity-depth pseudo-sections from coincident loop and in-loop TEM data, *Exploration Geophysics* 20(2) 43-45.
- Galley, A.G., Hannington, M. D., and Jonasson, I.R. (2007). Volcanogenic massive sulphide deposits, in Goodfellow, W.D., ed., *Mineral deposits of Canada: A Synthesis of Major Deposit-Types, District Metallogeny, the Evolution of Geological Provinces, and Exploration Methods*: Geological Association of Canada, Mineral Deposits Division, Special Publication No. 5, p. 141–161.

Geology map of Newfoundland and Labrador, (n.d.) gov.nl.ca. Retrieved from <https://www.gov.nl.ca/iet/files/mines-maps-nf.pdf>

Geotech Ltd. Report (2012). A helicopter-borne Versatile Time Domain Electromagnetic (VTEM) and horizontal magnetic gradiometer geophysical survey, Cripple Creek Property Gander, Newfoundland for 0840559 Ltd. by Geotech Ltd. (Report no. 12103).

Holladay et. al. (2006) UXO Time-Constant Estimation from Helicopter-Borne TEM data, JEEG, Volume 11, Issue 1, pp. 43-52.

In-phase and out-of-phase response of a sphere, (n.d.) em.geosci.xyz. Retrieved from [https://em.geosci.xyz/content/maxwell3\\_fdem/circuitmodel\\_for\\_eminduction/index.html](https://em.geosci.xyz/content/maxwell3_fdem/circuitmodel_for_eminduction/index.html)

Interface Conditions, (n.d.). em geosci. Retrieved from [https://em.geosci.xyz/content/maxwell1\\_fundamentals/interface\\_conditions/derivation.html#components-normal-to-the-interface](https://em.geosci.xyz/content/maxwell1_fundamentals/interface_conditions/derivation.html#components-normal-to-the-interface).

Lelièvre P. G. (2003). Forward Modelling and Inversion of Geophysical Magnetic data (Master's Thesis, University of British Columbia).

Lenters, M. H. (1988). Second-year assessment report on diamond drilling exploration for licence 2793 on claim blocks 3942-3944 and 4629-4631 in the Weirs Pond area, northeastern Newfoundland. Esso Minerals Canada Unpublished report.

Macnae et. al. (1991). Conductivity-depth imaging of airborne electromagnetic step-response data, SEG library, Volume 56, No 1, p. 102-114.

McNeill J. D. (1990) Use of Electromagnetic Methods for Groundwater Studies, Editor, Society of Exploration Geophysicist.

Nabighian M. N. and Macnae J.C. (1992) Electromagnetic Methods in Applied Geophysics Volume 2.

Nahnybida T. and Willet B. (2013). 2012 Assessment Report of Geological, Geophysical and Geochemical Exploration on Cripple Creek Property, Department of Natural Resources of Newfoundland Labrador Canada.

Oldenburg D. W. (1990). Inversion of Electromagnetic Data: An Overview of New Techniques, Department of Geophysics and Astronomy, U.B.C. Vancouver, Canada, V6T 1W5.

Oldenburg, D. W., and Li, Y. (2005). Near-surface geophysics, SEG investigations in geophysics. Vol. 13. Ch. Inversion for applied geophysics: a tutorial, pp. 89-150.

Pat Shanks, W.C., and Thurston, R. (2010). Volcanogenic Massive Sulphide Occurrence, Scientific Investigation Report 2010-5070-C, U. S. Geology Survey.

Swinden H.S. et al. (1990). Metallogenic Framework of Base and Precious Metal Deposits, Central and Western Newfoundland, Field Trip 1, Geological Survey of Canada, Open File 2156, p. 165-172.

EMIT (2016) The Program Maxwell, [electromag.com.au](http://electromag.com.au)  
<https://www.electromag.com.au/maxwell.php>

Ward S.H. and Hohmann G.W. (1988) Electromagnetic theory for geophysical applications, in Electromagnetics Methods in Applied Geophysics, V. 1, M.N. Nabighian, Editor, Society of Exploration Geophysicist.

Willet B. (2014). 2013 Assessment Report of Diamond Drilling on Licences of 167272M, 18072M, and 18923M, Cripple Creek Property, Northeastern Newfoundland for 0840559 B. C. Ltd.

Yang D. (2014). Geophysical Survey Decomposition and Efficient 3D Inversion of Time-Domain Electromagnetic Data (Doctor of Philosophy, The University of British Columbia).

## **Appendix A**

### **1D TEM inversion results as 2D cross-sections**

The 15 survey lines' inversion results are presented from L2140 to L2440 with 200m line spacing (see Fig. 5.5 for the locations of the survey lines).



